

1 Drone-based vertical profiling of particulate matter size 2 distribution and carbonaceous aerosols: urban vs. rural 3 environment

4 Kajal Julaha^{1,2,*}, Vladimír Ždímal², Saliou Mbengue³, David Brus⁴, Naděžda Zíková^{2,5,*}

5 ¹Department of Atmospheric Physics, Faculty of Mathematics and Physics, Charles University, Prague, 18000,
6 Czech Republic.

7 ²Institute of Chemical Process Fundamentals of the Czech Academy of Sciences, Prague 16500, Czech Republic.

8 ³Global Change Research Institute of the Czech Academy of Sciences, Brno 60300, Czech Republic.

9 ⁴Atmospheric Composition Research, Finnish Meteorological Institute, Helsinki 00560, Finland.

10 ⁵Institute for Environmental Studies, Faculty of Sciences, Charles University, Prague, 12801, Czech Republic

11
12 *Correspondence to: zikova@icpf.cas.cz (N. Zíková), julaha@icpf.cas.cz (K. Julaha)

13 **Keywords:** Equivalent black carbon, vertical distributions, Drone, micro-aethalometer AE51, optical particle
14 counter, Aethalometer AE33, optical particle sizer, humidity control.

15 **Abstract.** The study presents drone-based measurements to investigate the seasonal vertical variability of
16 equivalent black carbon (eBC) mass and particle number concentrations (PNC) at a rural and urban site in the
17 Czech Republic. Vertical profiles of eBC were measured using a micro-aethalometer, while PNC was measured
18 using an optical particle counter. Drone-based eBC measurements closely matched reference aethalometers placed
19 at both ground level and at 230m of a tower when using a humidity control mechanism. Without dryer, eBC mass
20 concentration was overestimated by 276% in summer and 285% in winter, but uncertainties were reduced to under
21 10% with drying. These findings highlight the importance of humidity control for accurate aerosol measurements,
22 especially for eBC. The study also revealed a decrease in eBC and PNC with height at the rural site during both
23 summer and winter, with seasonal differences in the altitude where this decrease began. Elevated eBC
24 concentrations in winter were due to increased atmospheric stability and combustion-related fine particles. At the
25 urban site, concentrations in summer were uniform with height (4 to 100 m AGL) but gradually decreased with
26 height during winter. Furthermore, the study investigated changes in the vertical distribution of eBC and PNC
27 during a high pollution event at the urban site, influenced by long-range transport. Our findings confirm the
28 effectiveness of drones in capturing vertical variations of air pollutants, offering results on the dynamics between
29 local emissions, atmospheric stability, and long-range transport and suggesting the necessity of measuring vertical
30 concentration profiles to support air quality management strategies.

31 1. Introduction

32 Black Carbon (BC) aerosols, one of the substantial contributors to climate change and adverse health effects, are
33 primarily emitted into our atmosphere through incomplete combustion of fossil fuels and biomass (Bond et al.,
34 2013; Ramanathan and Carmichael, 2008). BC absorbs efficiently solar radiation and contributes to atmospheric
35 warming (Moteki, 2023; Myhre et al., 2013). Aged BC can act as cloud condensation nuclei (CCN) and affect
36 climate through its indirect effects by altering cloud properties and their formation processes (Wang et al., 2018c).
37 The radiative properties of BC depend on its vertical profiles (Samset et al., 2013). For example, BC in the free
38 troposphere can enhance its radiative forcing by trapping energy emitted from the lower cloud layers (Schwarz et
39 al., 2006). The vertical distribution of BC also impacts the evolution of the planetary boundary layer (PBL). BC

40 in the upper PBL exhibits light absorption efficiency, heating the surrounding atmosphere and enhancing
41 atmospheric stability, leading to extreme haze pollution events (Ding et al., 2016).

42 Modeling-based studies on BC vertical distribution are limited (Chen et al., 2022). Uncertainties in these
43 models mainly arise from assumptions about the vertical distribution of BC aerosols, highlighting the need to
44 measure the vertical distribution of BC on a regional scale, from areas influenced by direct emissions from the
45 ground to those characterized by long-range transport (Ramana et al., 2010). These measurements can also help
46 validate satellite observations and improve the representation of BC vertical profiles in climate models, leading
47 to a more accurate assessment of BC radiative forcing (Li et al., 2013; Samset et al., 2013).

48 The BC vertical distribution can be measured by various platforms, such as meteorological balloons,
49 towers, aircraft, and unmanned aerial vehicles (UAVs). Meteorological tethered balloons provide highly resolved
50 data and detailed information close to the ground, capable of measuring aerosol concentrations up to the free
51 atmosphere (Babu et al., 2011; Ferrero et al., 2019; Renard et al., 2020; Cappelletti et al., 2022). Meteorological
52 towers offer a unique opportunity for continuous long-term monitoring of aerosols at different heights (Chi et al.,
53 2013; Xie et al., 2019; Sun et al., 2020; Liang et al., 2022). Compared to towers, aircraft and UAVs can access
54 higher altitudes, with some aircraft capable of carrying heavier payloads, allowing them to transport more
55 sophisticated instruments for detailed aerosol measurements. These platforms offer greater spatial coverage and
56 flexibility, making them suitable for comprehensive atmospheric studies (Brady et al., 2016; Corrigan et al., 2007;
57 Villa et al., 2016; Wu et al., 2021; Schulz et al., 2019). Drones have recently gained popularity among all the other
58 methods because of their cost effectiveness, flexibility, and mobility due to their lightweight design (Barbieri et
59 al., 2019; Boer et al., 2020). Several studies have used drones to study vertical measurements of BC and particle
60 number concentrations (PNC). For example, Liu et al. (2020) conducted vertical measurements of fine particulate
61 matter (PM) and BC using a DJI Matrice 600 drone equipped with a battery-operated light-scattering laser
62 photometer and a micro-aethalometer. Their study revealed different vertical patterns for PM2.5 and BC,
63 suggesting different sources for each. Similarly, Zhu et al. (2019) used a hexacopter with a customized scanning
64 mobility particle sizer, an optical particle counter, and a meteorology sensor to study the vertical variability of
65 particle number size distribution (PNSD) near the ground to up to 300 m. The study showed that PNC with size
66 $>0.3 \mu\text{m}$ decreased with height during the evening. Brus et al. (2021) investigated the vertical profile of PNCs and
67 gases in the San Luis Valley, Colorado, and highlighted their interaction with meteorological conditions and
68 boundary layer processes. Studies on the vertical distribution of BC aerosols in Central Europe are very limited.
69 In Poland, Chilinski et al. (2016) examined the vertical distribution of BC in a valley for three days using UAV.
70 In Germany, Samad et al. (2020) investigated the vertical profiles of PM, BC, and ultrafine particles in Stuttgart
71 using a tethered balloon, and Harm-Altstädtter et al. (2024) used a fixed-wing drone for vertical measurement of
72 aerosol concentration, including eBC, near a civil airport.

73 The studies about the vertical distributions of BC aerosols in the Czech Republic are limited to a tall
74 tower in a rural area (Mbengue et al., 2023), and no measurements in urban areas have been done. To date, no
75 drone-based measurement of BC has been conducted in the Czech Republic. This study combines mobile (drone-
76 based) and fixed (tall tower and building) observational platforms to measure the vertical distribution of BC
77 aerosols and PNC at two different sites representing an urban and a rural location to isolate the respective roles of
78 local emissions, meteorology, and long-range transport in shaping vertical aerosol distributions. It further

79 estimates the measurement uncertainties and dependence of the results on the humidity. In this study, we address
80 this gap by developing and testing a lightweight, drone-mountable silica-gel dryer that enables humidity-
81 controlled eBC measurements.

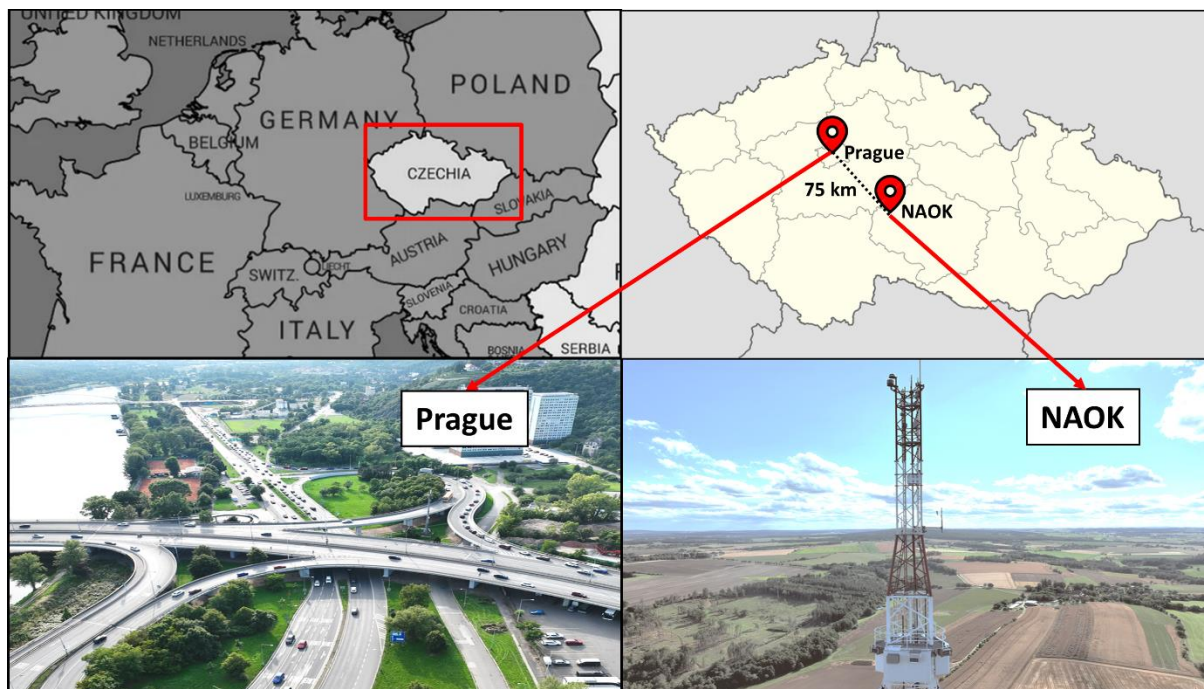
82 **2. Materials and Methodology**

83 **2.1. Measurement Sites**

84 **2.1.1. Rural background site**

85 The National Atmospheric Observatory Košetice (NAOK, $49^{\circ}35'N$, $15^{\circ}05'E$; 534 m a.s.l.) in the Bohemian
86 Moravian Highlands in the Czech Republic (Figure 1) represents a central European background site. Located
87 approximately 75 kilometers southeast of Prague, the observatory is situated in a rural area. The observatory is
88 equipped with instruments to measure gaseous pollutants, atmospheric aerosols, and meteorological parameters.
89 It includes a 250 m tall atmospheric tower which provides a unique opportunity to study atmospheric parameters
90 at different elevations (Dvorská et al., 2015). NAOK is part of the Aerosol, Clouds, and Trace Gases Research
91 Infrastructure Network (ACTRIS ERIC) and several other research projects and monitoring programs (Mbengue
92 et al., 2023).

93 NAOK is influenced by regional and long-range transported air masses, mainly associated with the
94 western and southeastern directions (Mbengue et al., 2021; Vodička et al., 2015). A primary highway in the Czech
95 Republic (D1: 36,000 cars/day, CSD, 2020) is situated approximately 6 km to the north and northeast of the
96 observatory (Mbengue et al., 2023).



97 **Figure 1. Geographical location of rural background (NAOK) and urban (Prague) sites in the Czech Republic. Source:**
98 **mapchart.net, Wikipedia.**

100 **2.1.2. Urban site**

101 The Faculty of Mathematics and Physics (50°6.89'N, 14°26.95'E; 185 m a.s.l.) at Charles University in Prague
102 represents an urban site situated 75 kilometers away from NAOK (Figure 1). The faculty has multiple campus
103 locations throughout Prague, with its Troja campus near the Vltava River serving as the site for this study. The
104 main building of the Troja campus is an 11-story building, almost 50 m high. The campus is located in a river
105 valley surrounded by hills with an elevation of 50 m AGL. The Department of Atmospheric Physics (DAP) is also
106 on this campus. The DAP monitors particulate matter (PM₁, PM_{2.5}, and PM₁₀), gases (NO₂, O₃, and CO), and
107 meteorology (temperature, relative humidity (RH), pressure, wind speed, and rainfall), with measurements taken
108 at ground level (2m), 10 m, and 50 m (Ramatheerthan et al., 2024).

109 The site is located near the Blanka tunnel exit and is impacted by fresh traffic emissions. The Blanka
110 tunnel, more than 6 km long, is the longest road tunnel in the Czech Republic. The average traffic density of this
111 tunnel is 80,000 to 90,000 cars/day (Metrostav, 2024). It was constructed to minimize the environmental impacts
112 of traffic. However, its opening significantly increased the traffic at some locations, leading to substantial changes
113 in the urban geochemistry of Prague (Mizera et al., 2022).

114 **2.2. Instrumentation**

115 **2.2.1. eBC measurements**

116 The micro-Aethalometer AE51 (AethLabs San Francisco, CA) (Figure 2a) provides real-time equivalent BC
117 (eBC) concentration using an 880 nm light source (Petzold et al., 2013). AE51 operates on a principle similar to
118 other aethalometers, such as AE31 (Aerosol Magee Scientific, Berkeley, CA). The AE51 measures the light
119 attenuation through a filter (T60 Teflon-coated glass fiber) loaded with particles and converts the attenuation into
120 an eBC mass concentration using a predefined mass attenuation coefficient (12.5 m²/g) (Alas et al., 2020). The
121 time resolution of 10 seconds and flow rate of 150 ml/min were used in this study. The filter was replaced when
122 attenuation, a dimensionless measure of optical absorbance, reached 80 to minimize the filter loading effect. This
123 threshold has been recommended to reduce measurement bias due to increasing filter loading (Good et al., 2017;
124 Lee, 2019; Miyakawa et al., 2020). Recent studies (Alas et al., 2020; Masey et al., 2020) have shown that
125 uncorrected AE51 readings closely match reference instruments in low-concentration environments. Therefore,
126 no correction method was used for the eBC values in the present study.

127 To reduce short-term noise, AE51 data were averaged over 1-minute intervals. If the resulting mean eBC was
128 negative, the measurement point was excluded from further analysis. The fraction of excluded data was below 2%
129 for all periods except the NAOK summer, where it reached a maximum of 10% at altitudes above 100 m.

130 **2.2.2. Air stream Dryer**

131 A 20 cm-long homemade silica gel dryer (Figure 2d) was used in front of the AE51 (Figure 2f) to control the
132 humidity for accurate eBC mass concentration measurements. The dryer consists of 2 coaxial cylinders of 1.62
133 cm and 0.65 cm diameters, with silica gel in the space between them. The silica gel effectively removes moisture
134 from the aerosols as axial airflow passes through the dryer. The silica gel used in the dryer was spherical bead-
135 type (Carl Roth, P077.1, “Perfform”), which is mechanically robust and non-dusting, minimizing any risk of
136 particle shedding under vibration. Additionally, the dryer was sealed with stainless-steel mesh (inner cylinder) at

137 both ends to prevent the possible release of silica fragments during operation. The inner cylinder (diameter 6.6
138 mm and length 13.5 cm), of stainless steel woven mesh screen with a 0.25 mm x 0.25 mm square hole aperture
139 (80 opening per inch, 0.05 mm wire, ~65 % open area), was chosen for its smooth surface and minimal particle
140 loss, while the outer parts were fabricated with PLA (Polylactic Acid) using a 3D printer (MK4S, Prusa Research),
141 with a total weight of 50 g. Particle loss was evaluated using the Particle loss calculator (von der Weiden et al.,
142 2009) and found to be $\leq 1\%$ for PM2.5-sized particles at the AE51's flow rate of 150 mL/min (Table S2). The
143 performance of the dryer was tested in laboratory conditions by passing air with 100% RH through the setup at
144 the AE51's flow rate of 150 mL/min. The dryer effectively reduced the RH to below 40%, and maintained that
145 level for up to 3 days, ensuring reliable drying under operational flow (Figure S1). The silica-gel beads were
146 replaced every morning before measurements began. The flow and leakage tests were also carried out to describe
147 the dryer's performance at 150 mL/min. The flow rate was monitored before and after the dryer using a mass flow
148 meter. For the leak test, the dryer inlet was connected to a HEPA filter, and the outlet was connected to a
149 Condensation Particle Counter (CPC) to monitor any particle breakthrough. Particle concentrations measured by
150 the CPC were found to be negligible, confirming the air-tight integrity of the dryer assembly.

151 **2.2.3. Particle number concentration measurements**

152 The air quality measurements backpack (Yugen Oy, Finland) for a consumer-grade drone with an Optical particle
153 Counter (OPC-N3, Alphasense) (Figure 2b) was used to measure PNC in the polystyrene latex (PSL) equivalent
154 size range from 0.35 to 40 μm . The OPC detects the light scattered by particles in the sample air stream illuminated
155 by a laser beam (~658 nm) and translates the signal into particle count and size (Hagan and Kroll, 2020). The
156 OPC-N3 reports an internal airflow estimate based on a low-power internal fan performance, not corrected for
157 external wind. The OPC's inlet was horizontally mounted and exposed to wind during drone flights so that it faced
158 oncoming airflow. While this minimized directional variability, strong horizontal winds could still affect the
159 internal airflow stability of the OPC-N3 (Table S2). To mitigate this, all measurements were averaged over 1-
160 minute intervals, which helps reduce short-term fluctuations. Due to OPC's horizontal inlet design and a low
161 power built-in ventilator, equipping a dryer would result in an excessively high pressure drop (manufacturer's
162 maximum allowable pressure drop ≤ 40 Pa), making the measurement highly unreliable (Bezantakos et al., 2020)
163 and thus the OPC-N3 was operated without a dryer. Since OPC-N3 sampled air without drying, the measured
164 particle sizes and number concentrations may therefore be affected by hygroscopic growth under high relative
165 humidity conditions. However, the instrument's internal T is slightly elevated due to electronics heat emission,
166 reducing the humidity of the sampled air. Analysis of the internal RH logs revealed that no data exceeded 80%
167 RH, and most measurements were taken under relatively dry conditions (RH $< 40\%$ in 60–90% of cases,
168 depending on the season and height). Therefore, hygroscopic growth effects were expected to be minor. Similar
169 limitations and evaluation strategies (flagged RH $> 80\%$) have been documented in previous UAV-based OPC
170 studies (Brus et al., 2025; Chacón-Mateos et al., 2022; Nurowska et al., 2023; Nurowska and Markowicz, 2023)."

171 The backpack with OPC uses a Raspberry Pi zero microcomputer as a data logger and was mounted on
172 the top of the drone (Figure 2g). The backpack also contains two meteorological sensors BME 280 (Bosch
173 Sensor tec GmbH) and SHT85 (Senserion AG) positioned on opposite side of the backpack (see their comparison
174 in the next section) and a redundant to drone own GPS module for the recording of drone position (Brus et al.,
175 2025). The backpack housing was 3D-printed using white polyethylene terephthalate glycol (PETG) filament,

176 which provides structural support and helps reflect solar radiation to minimize thermal influence on the sensors.
177 The dual-sensor configuration also reduces bias caused by asymmetric solar heating, which can lead to small
178 temperature differences (up to a few degrees) under clear-sky conditions, while remaining negligible under
179 overcast skies. Temperature and RH readings from both sensors were compared against tower-based temperature
180 and RH data while flying on the drone at different heights to evaluate the feasibility and reliability of using the
181 drone-based setup for vertical profiling of temperature and RH validate sensor accuracy and data reliability (Figure
182 S2-S5).

183 The total particle number concentration (N), in particles per cubic meter (#/m³), was calculated from the
184 raw OPC data as:

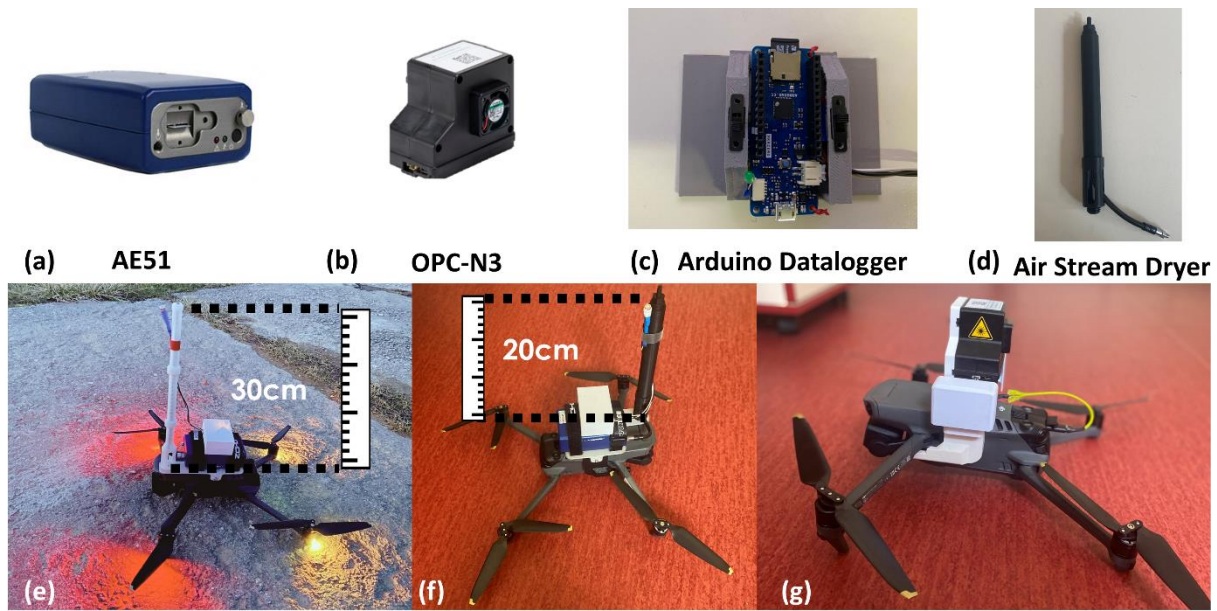
$$185 N = \frac{C}{F \cdot t}, \quad (1)$$

186 where C is the total particle count, F is the flow rate in cm³/s, and t is the sampling time in seconds. The OPC
187 operates at a total flow rate of 5.5 l/min and a sample flow rate of 0.28 l/min. The measurement interval of 1
188 second was used to account for the high temporal variability of particles' concentrations.

189 **2.2.4. Temperature and RH**

190 For OPC, sensor SHT85 was used to measure ambient temperature (T) and RH, while with AE51, an Arduino
191 (MKR Zero) datalogger (HYT939p, Innovative Sensor Technology IST AG) (Figure 2c) was used for T and RH
192 measurements. Although HYT939p has a slower nominal response time (\approx 2–3 s), potential lag effects were
193 negligible because the drone hovered for approximately 5 min at each altitude and data were averaged over 1-min
194 intervals. The HYT939P showed close agreement with tower-based T/RH measurements (see Figures S6 and S7
195 and Table S3), confirming its suitability for UAV-based profiling. The Arduino MKR zero microcontroller
196 processes sensor data using a 32-bit SAMD21 processor and stores it on an SD card. It is programmed via the
197 Arduino IDE to read inputs, perform tasks, and save data. The Arduino datalogger with HYT939p sensor was
198 developed after the first summer campaigns at both sites and, therefore, was used only during winter campaigns.
199 For the summer campaign, meteorological variables from the tower at the same height as the drone hover at
200 NAOK were used, and in Prague, meteorological data from the ground and top of the building, i.e., 50 m, were
201 used.

202 UAV-based T and RH measurements showed strong agreement with tower observations ($R^2 = 0.85$ –0.99
203 for T and 0.50–0.96 for RH; RMSE = 0.3–2.4 °C and 5–8 %, respectively, Figure S2-S7). Among the sensors, the
204 HYT939p exhibited the most stable performance and the smallest bias, while the SHT85 and BME showed largest
205 scatter (Figure S8 and Table S3). On average, UAV readings were \sim 0.3 °C warmer and \sim 7 % drier than the tower
206 reference. The moderate reduction in correlation above 150 m, primarily due to fewer data points and a response
207 lag at 230 m, reflects the known limitations of compact airborne sensors (Brus et al., 2025). These uncertainties,
208 however, remain within acceptable limits for UAV-based meteorological measurements, as demonstrated in
209 previous intercomparison studies (Barbieri et al., 2019).



210

211 **Figure 2. Measurement setup:** (a) micro-Aethalometer AE51, (b) optical particle counter (OPC) N3, (c) Arduino
 212 datalogger, (d) Air Stream Dryer, (e) micro-Aethalometer AE51 with a temperature and RH datalogger without a
 213 dryer, (f) micro-Aethalometer AE51 with a temperature and RH datalogger with a dryer, and (g) consumer drone
 214 backpack with an optical particle counter with a custom mount on the drone.

215 **2.2.5. Drone-based sampling**

216 The instruments were installed on the Mavic 3 Classic drone (DJI Techology Co., Ltd.)
 217 (<https://www.dji.com/cz/mavic-3-classic/specs>). The instrument's combined weight was too high to be carried by
 218 the drone; thus, the instruments were set up separately and measured each alternating hour under similar
 219 meteorological conditions.

220 With the micro-Aethalometer AE51, two different types of inlets were used: a 30 cm high inlet without
 221 a dryer and a 20 cm high inlet with a diffusion-based silica gel dryer, while no inlet was used with a drone
 222 backpack (Figure 2). In the dryer-equipped setup, in contrast to the non-dryer configuration using a single bend
 223 (Figure 2e), an additional 90° bend in the inlet tubing was necessary to accommodate the dryer housing (Figure
 224 2f). Based on an equivalent pipe length (EPL) of 0.15 m per 90° bend (radius < 5 cm; Wang et al., 2002), the EPL
 225 increased from 42 cm (without dryer) to 49 cm (with dryer). The AE51's sampling height and mounting position
 226 remained unchanged, and this small difference in EPL is negligible for submicron aerosols at 0.15 L min⁻¹ (von
 227 der Weiden et al., 2009).

228 Particle losses within the AE51 inlet system were estimated using the Particle Loss Calculator (von der
 229 Weiden et al., 2009) for all measurement configurations and wind speeds (Table S2). For a 30 cm high inlet
 230 without dryer, total transmission efficiency for particles $\leq 2.5 \mu\text{m}$ corresponded to losses $\leq 9 \%$, while for the
 231 20 cm dryer inlet, losses were $\leq 1 \%$. Whole-inlet losses were evaluated for both AE51 configurations (with and
 232 without dryer) to assess the effect of wind speed on sampling accuracy. For the AE51 without dryer, concentration
 233 changes for PM_{2.5} remained minimal (< 10 % overestimation) up to 4 m s⁻¹ but increased at higher wind speeds,
 234 reaching about 22 % overestimation for PM₁ at 6 m s⁻¹. When the dryer was attached, the sampling efficiency also

235 decreased with wind speed, with overestimation increasing from ~5 % at 2 m s⁻¹ for PM₁ to ~50 % at 6 m s⁻¹ for
236 PM_{2.5}.

237 Only sampling losses were calculated for OPC and OPS, as no inlet extension was used. For OPS,
238 sampling loss was minimal (10 % overestimation) for PM_{2.5} fraction up to wind speed of 6 m/s, but PM₁₀ showed
239 an underestimation of 100 % up to 6 m/s. For OPC, sampling effects were less severe (50 % overestimation up to
240 6 m/s) for PM₁, but for PM_{2.5}, overestimation ranged from 60 % to 125 % at 4 m/s and 6 m/s, respectively. For
241 PM₁₀ particles, overestimation was as high as 750% at 6 m/s.

242 During the flights, the drone climbed vertically from the ground to 230 m and 100 m AGL at a constant
243 speed of 1 ms⁻¹ along the tower at NAOK and the Prague building, respectively (the maximum altitude was limited
244 to 100 m in Prague due to flight height restrictions). The drone hovered at different heights (4 m, 50 m, 100 m,
245 150 m, and 230 m at NAOK and 4 m, 50 m, and 100 m in Prague) for at least 3-5 minutes and then ascended in
246 the same vertical direction. To reduce short-term noise, the raw data were averaged into 1-minute intervals,
247 yielding 3–5 values per altitude per flight. Although continuous measurements were recorded during each ascent
248 flight, only hovering measurements at different heights were used in this study. This approach reduces the
249 influence of rotor-induced turbulence and enables more stable sampling conditions. While ascent and hovering
250 show a 3–6 % error in particle concentration, the descending flights were excluded due to the propellers-induced
251 airflow increasing apparent particle concentrations by up to 40–60% (Hedworth et al., 2022).

252 Flights were conducted for at least 4 to 5 days during a week, depending on the weather conditions.
253 Across the full campaign (approximately 15–20 flights), these 1-minute averages were grouped by altitude, and
254 the resulting distributions were used for comparisons with reference instruments (e.g., AE33) and visualized at
255 each height level.

256 To compare OPC-N3 (0.35–37 µm measurement size range) with the OPS (0.3–10 µm size range), size-
257 bin harmonization was applied. For each 1-min average, OPC binned number concentrations were linearly
258 interpolated in log₁₀(D_p) space from OPC mid-bin diameters onto the OPS bin grid over the overlapping size range
259 of 0.35–10 µm (Weltje and Roberson, 2012). For all other analyses and plots, no bin harmonization was applied
260 and data are presented in the full size ranges.

261 The summer campaign took place at NAOK from July and August 2023, and the winter campaign in
262 February 2024 (Table 1). Additionally, a test to evaluate the dryer's performance was conducted on August 13,
263 2024. The dryer-on intercomparison at NAOK was performed on a single day. In Prague, measurements were
264 performed during two summer campaigns and one winter campaign across 2023 and 2024. The urban
265 measurements were taken without a dryer in August 2023, and in December 2023, while a dryer was used for eBC
266 measurements in July 2024 (Table 1). Measurements for each campaign began at 06:00 UTC (08:00 CEST) and
267 continued until 18:00 UTC (20:00 CEST) during the summer, and from 07:00 UTC (08:00 CET) to 16:00 UTC
268 (17:00 CET) during the winter, due to shorter daylight hours. The number of flights for eBC and PNC at each
269 height is summarized in Table 1.

270 **Table 1. Overview of campaign schedule and total number of flights for eBC and PNC measurements. Campaigns with**
271 **a dryer are indicated with an asterisk.**

	Season	Campaign Dates	Number of flights (eBC)	Number of flights (PNC)	Measurement height (m AGL)
NAOK	Summer	July 31 to August 4, 2023	20	18	4,50,100,150,230
	Summer*	August 13, 2024*	12*	---	4*,230*
	Winter	February 12 to 16, 2024	15	15	4,50,100,150,230
Prague	Summer	August 14 to 20, 2023	22	21	4,50,100
	Summer*	July 18 to 23, 2024*	21*	21*	4*,50*,100*
	Winter	December 12 to 18, 2023	17	17	4,50,100

272

273 **2.2.6. Additional variables**

274 At NAOK, two aethalometers AE33 were available as reference instruments: one at the ground with a PM₁₀
 275 sampling inlet (Leckel GmbH) at 4 m AGL and the other installed at the top of the tower, i.e., at 230 m with the
 276 same sampling head as on the ground. The data from these aethalometers were compared with the drone-based
 277 measurements while the drone hovered at corresponding heights. The AE33 at the ground uses a Nafion dryer
 278 (custom-made, TROPOS, Leipzig, Germany) to remove moisture from the sample stream, whereas AE33 at 230
 279 m was connected to a Nafion dryer but was not supplied with dry air during the summer of 2023 and winter
 280 campaigns. An Optical Particle Sizer (OPS) (model 3330, TSI Inc., USA), without any dryer to ensure similar
 281 measurement conditions, was placed at 4 m for comparison with the measurement from OPC on the drone. In
 282 addition, temperature, RH, global radiation, wind speed and direction, and gaseous concentrations were obtained
 283 from standard measurements at multiple tower heights (50 m, 125 m, and 240 m) and ground level (4 m) (Dvorská
 284 et al., 2015), and ceilometer CL51 (Vaisala, Finland) was used for every hour boundary layer height (BLH)
 285 information (Julaha et al., 2025) at NAOK..

286 In Prague, long-term measurements alongside the building include data on temperature, RH, wind speed,
 287 gaseous concentrations, and particulate matter concentrations, monitored at ground level, 10 m, and at the top of
 288 a 50m high building (Table 2) (Ramatheerthan et al., 2024). Since ground-based ceilometer measurements for the
 289 BLH were not available at the site, boundary layer height predictions were obtained from ERA5, a fifth-generation
 290 ECMWF (European Centre for Medium Weather Forecasting) reanalysis model produced by the Copernicus
 291 Climate Change Service (C3S). The hourly boundary layer height was obtained for the duration of campaigns
 292 (Hersbach et al., 2023). The consistency between ERA5-derived and ceilometer-observed BLH values was
 293 previously assessed (Julaha et al., 2025), showing good agreement at NAOK. Consequently, ERA5 data were
 294 considered reliable for estimating BLH at the urban site.

295 Normality was evaluated using the Shapiro–Wilk test ($p < 0.05$). Since the data were non-normally
 296 distributed, the Kruskal–Wallis test was used to determine significant differences in eBC (and PNC)
 297 concentrations between sampling heights. Sample sizes (N) are shown on boxplots. All groups had $N \geq 10$,
 298 satisfying the minimum requirement ($N > 5$) for reliable Kruskal–Wallis testing of small, non-normal datasets
 299 (Sheskin, 2003).

300 The percentage difference (PD) was calculated to evaluate variability across measurements for
 301 comparing data across different heights and conditions:

302
$$PD = \frac{X_{ref} - X_{drone}}{X_{ref}} * 100, \quad (2)$$

303 where X_{ref} is concentration from reference device and X_{drone} is concentration from device on drone. The same
304 approach was taken also for calculating the difference between heights.

305 The wind shear between the heights was calculated as the difference in wind speed (ΔWS) divided by
306 the difference in altitude (Δz):

307
$$Wind Shear = \frac{\Delta WS}{\Delta z}, \quad (3)$$

308 given in m/s per 100 m.

309 **Table 2. Variables and instrumentation used in this study.**

	Instruments	variables	Measurement heights (m AGL)	
			NAOK	Prague
Drone	AethLabs AE51	eBC	4, 50, 100, 150, 230	4, 50, 100
	Alphasense OPC N3	PNC	4, 50, 100, 150, 230	4, 50, 100
	BME and SHT85	T, RH, P	4, 50, 100, 150, 230	4, 50, 100
	Arduino HYT939p	T, RH	4, 50, 100, 150, 230	4, 50, 100
	Drone (DJI Mavic 3 Classic)	ws	4, 50, 100, 150, 230	4, 50, 100
Fixed	Magee AE33	eBC	4, 230	-
	TSI OPS 3330	PNC	4	-
	Vaisala Ceilometer CL51	BLH/MLH	ground	-
	Tower measurements	T, RH, P, ws, wd	10, 50, 125, 240	-
	ENVISENS M-22-017	Global Radiation	ground	50
	Envitech ED-19-004, ED-19-005	PM	-	10, 50
	Aeroqual AQS1, Envitech M-22-016, M-22-017	NO ₂ , O ₃ , CO	-	2, 50
	Davis Vantage Pro2, Meteopress MD1017, MD1016	T, H, P, ws	-	10, 50
	ERA5	BLH	-	-

310 **3. Results and Discussion**

311 **3.1. Intercomparison and effect of RH on eBC and PNC measurements**

312 To assess the reliability of drone-based aerosol observations, eBC and PNC measured while hovering the drone
313 were compared with the observations from the reference devices from the NAOK tower at 4m and 230m for both
314 the summer and winter campaigns. Because the reference instruments were available only at the NAOK site, the
315 validation of drone-based measurements based on 15 days of measurements was performed exclusively there,
316 providing basis for assessing instrument performance under real ambient conditions.

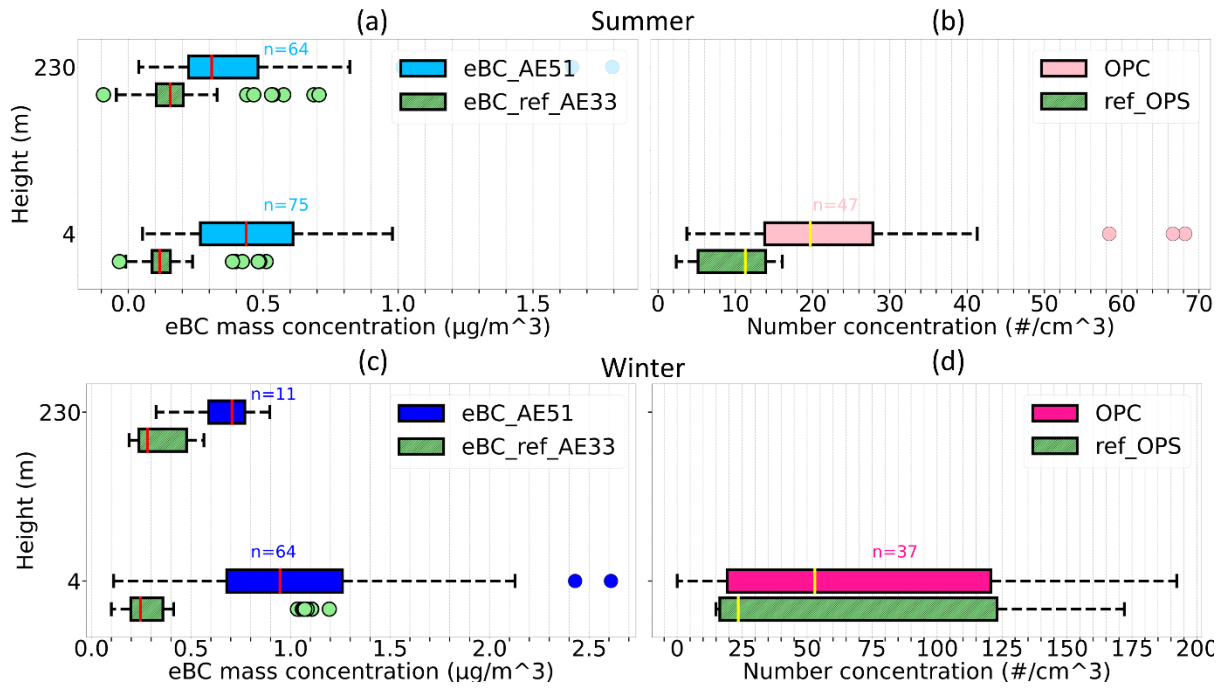
317 The AE51 on the drone overestimated the median reference eBC mass concentration by approximately
318 276 % at 4m and by 99 % at 230m during summer, with absolute differences of 0.32 $\mu\text{g}/\text{m}^3$ and 0.15 $\mu\text{g}/\text{m}^3$,

319 respectively. The smaller overestimation at the 230 m can be due to similar measurement conditions as both AE33
320 at 230 m and the AE51 on the drone were operating without any dryer (except Nafion without dry air in front of
321 the AE33, which may have partially influenced the moisture content of the sampled air). The higher difference at
322 4m during the summer is likely due to high RH affecting the eBC measurements; while a Nafion dryer was
323 installed in front of the AE33 on the ground, the AE51 on the drone without a dryer was strongly influenced. This
324 was further confirmed when the RH dropped below 40 % on 3 August, 2023, and eBC mass concentrations from
325 AE51 on the drone were comparable with the reference devices at both 4 m and 230 m, as indicated by Kruskal-
326 Wallis (KW) test showing no significant difference ($p > 0.05$) (Figure S9).

327 During the winter campaign, median drone-based measurements using AE51 overestimated eBC mass
328 concentrations by 285 % ($0.7 \mu\text{g}/\text{m}^3$) at 4 m and by 150 % ($0.4 \mu\text{g}/\text{m}^3$) at 230 m compared to the reference AE33
329 observations (Figure 3). This can be attributed again to the influence of humidity—at 4m, the AE33 was operated
330 with a dryer, and the temperature gradient between inside the measurement container and the external environment
331 at 230 m likely contributed to some drying effects as the sample travelled from the colder outdoor to the warmer
332 indoor environment.

333 The PNC from OPC on the drone also showed overestimation compared to the OPS reference
334 observations by 75 % ($8 \#/ \text{cm}^3$) and 129 % ($30 \#/ \text{cm}^3$) during summer and winter, respectively. The comparison
335 was made using the same size bins, with the interpolation applied to align the bins between the two instruments.
336 Both the OPC and OPS measurements were conducted without a dryer for both seasons, thus measuring aerosol
337 PNC at ambient RH. The observed difference can be attributed to different sampling orientations: OPC inlet
338 sampled horizontally against the wind, while OPS had a vertical inlet, causing different influence on sampling in
339 both instruments. For OPS, the sampling showed overestimation within 10 % for $\text{PM}_{2.5}$ up to wind speed of 6 m/s.
340 In contrast, for OPC, overestimation jumped to 60 % and 125 % for $\text{PM}_{2.5}$ at wind speeds of 4m/s and 6m/s,
341 respectively. As a result, OPC tends to report higher particle concentration than the OPS, which contributes to the
342 discrepancies observed in the PNC values. Furthermore, the absence of drying likely enhanced apparent particle
343 sizes during high-RH periods; however, internal OPC-N3 RH records indicate that all measurements were
344 performed at $\text{RH} < 80\%$. The slightly elevated internal temperature of the OPC reduces in-flow humidity, thereby
345 suppressing hygroscopic particle growth. Consequently, humidity-related artefacts were limited and do not affect
346 the interpretation of relative vertical and seasonal variability.

347



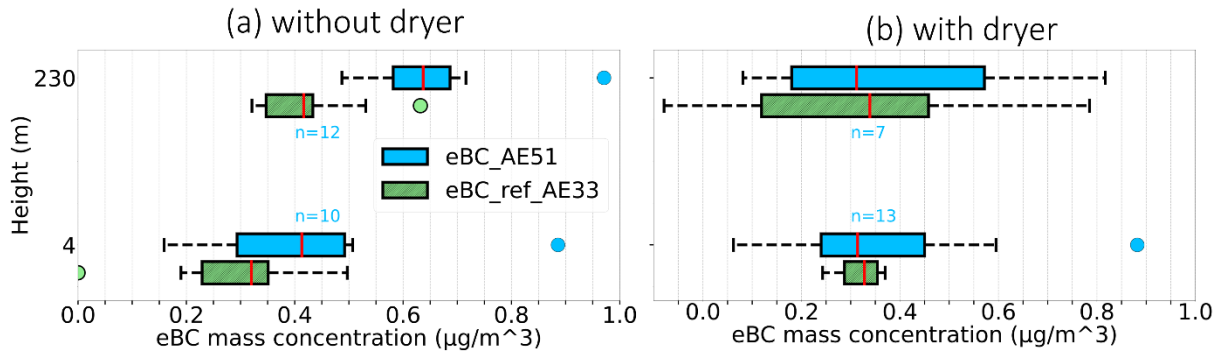
349 **Figure 3.** Boxplots of (a) eBC mass concentration and (b) PNC from drone vs. reference devices in the $0.35 - 10 \mu\text{m}$ size
350 range from the tower at 4 m and 230 m during the summer 2023 campaign at NAOK; c) and d) the same for winter
351 2024. Boxes show median and IQR; whiskers extend to $1.5 \times \text{IQR}$; points beyond are outliers. n = number of points (1-
352 min means) per altitude.

353 To address the effect of RH on eBC concentrations from drone measurements, a homemade silica gel
354 dryer was installed on the drone. A test to evaluate the dryer's performance was conducted on August 13, 2024,
355 a typical summer day with a temperature of 28°C , RH varying from 50% to 90%, and a wind speed of 2-3 m/s.
356 Additionally, the aethalometer on the top of the tower at NAOK was equipped with a nafion dryer to ensure
357 consistent comparison between the two AE33 at different levels and between AE33 and AE51 under varying RH
358 levels throughout the day. The eBC measurements were done with and without the dryer at the drone and
359 compared to the AE33 eBC concentrations at the tower (both with Nafion dryers).

360 During this particular summer day, the AE51 on the drone without the dryer overestimated eBC mass
361 concentrations by 29 % ($0.09 \mu\text{g}/\text{m}^3$) at 4 m and by 53 % ($0.22 \mu\text{g}/\text{m}^3$) at 230 m compared to the reference AE33
362 (Figure 4a). After installing the silica gel dryer on the drone, the eBC measurements were closely aligned with
363 the reference observations, with the difference reduced to under 10% ($0.01 \mu\text{g}/\text{m}^3$ at 4 m and $0.02 \mu\text{g}/\text{m}^3$ at 230
364 m) at both heights (Figure 4b). This highlights the significant role of the dryer in minimizing the humidity impacts
365 and enhancing the accuracy of eBC mass concentration measurements from the micro-aethalometer AE51. These
366 findings further confirm the reliability of the drone platform and its effectiveness in providing eBC measurements
367 that compare well with long-term tower observations. The AE51, like other single-spot aethalometers, can
368 respond to light-scattering aerosols. This effect was minimized by using a dryer and verified by the close
369 agreement with AE33 data, so any positive bias from non-absorbing particles was considered negligible.

370 The strong overestimation of eBC by the AE51 under high relative humidity is consistent with
371 hygroscopic growth of scattering aerosols, which increases apparent light attenuation (Cai et al., 2013). Water
372 uptake by soluble particles can amplify both scattering and absorption on the AE51's filter, artificially inflating

373 the reported eBC. This bias is especially problematic in mobile measurements, where the RH fluctuates rapidly.
 374 By installing a silica-gel dryer to maintain RH below $\sim 40\%$, the humidity-induced artifact was eliminated, and
 375 AE51 readings aligned well with reference AE33 measurements.



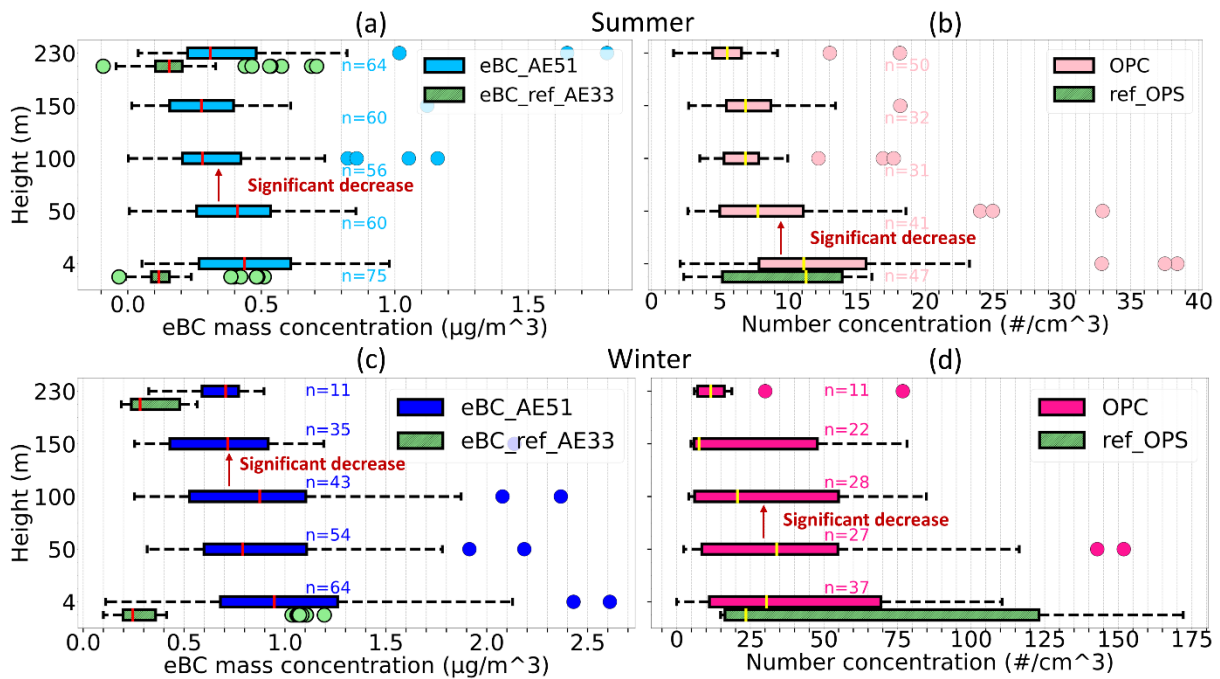
376
 377 **Figure 4. Boxplots of eBC mass concentration from drone and reference devices on the tower at NAOK during a**
 378 **summer day (August 13, 2024) at 4 m and 230 m (a) without the dryer and (b) with the dryer. Boxes show median and**
 379 **IQR; whiskers extend to $1.5 \times \text{IQR}$; points beyond are outliers. n = number of points (1-min means) per altitude.**

380 3.2. Aerosol vertical profile at the rural site

381 Vertical profiles of eBC mass concentrations without the silica gel dryer and PNC were measured while hovering
 382 the drone at different heights (4 m, 50 m, 100 m, 150 m, and 230 m) during the summer 2023 and winter 2024 at
 383 NAOK simultaneously with the reference instruments (Figure 5). During summer, eBC mass concentration
 384 remained relatively uniform up to the height of 50 m, followed by a decrease of 32 % ($0.13 \mu\text{g}/\text{m}^3$) between 50
 385 and 100 m. Conversely, PNC dropped by 30 % ($6 \#/cm^3$) between 4 m and 50 m. In winter, eBC mass concentration
 386 stayed constant up to 100 m and decreased by 18 % ($0.16 \mu\text{g}/\text{m}^3$) between 100 m and 150 m. PNCs were constant
 387 from the ground to 50 m but decreased by 39 % ($24 \#/cm^3$) between 50 m and 100 m. The significance of the
 388 increase or decrease in eBC mass concentration and PNC was tested by the Kruskal-Wallis (KW) test ($p < 0.05$).
 389 When plotted using native (non-interpolated) bins, the OPC-N3 and OPS show closer agreement (see Figure 5).

390 The general decrease of both eBC and PNC with height indicates that surface sources dominate aerosol
 391 loading at this rural site and that vertical mixing was insufficient to fully homogenize the boundary layer. Similar
 392 vertical gradients have been observed in background and rural settings, where limited turbulence allows
 393 combustion-derived fine particles to accumulate near the ground, resulting in declining concentrations aloft
 394 (Harm-Altstädtter et al., 2024; Samad et al., 2020).

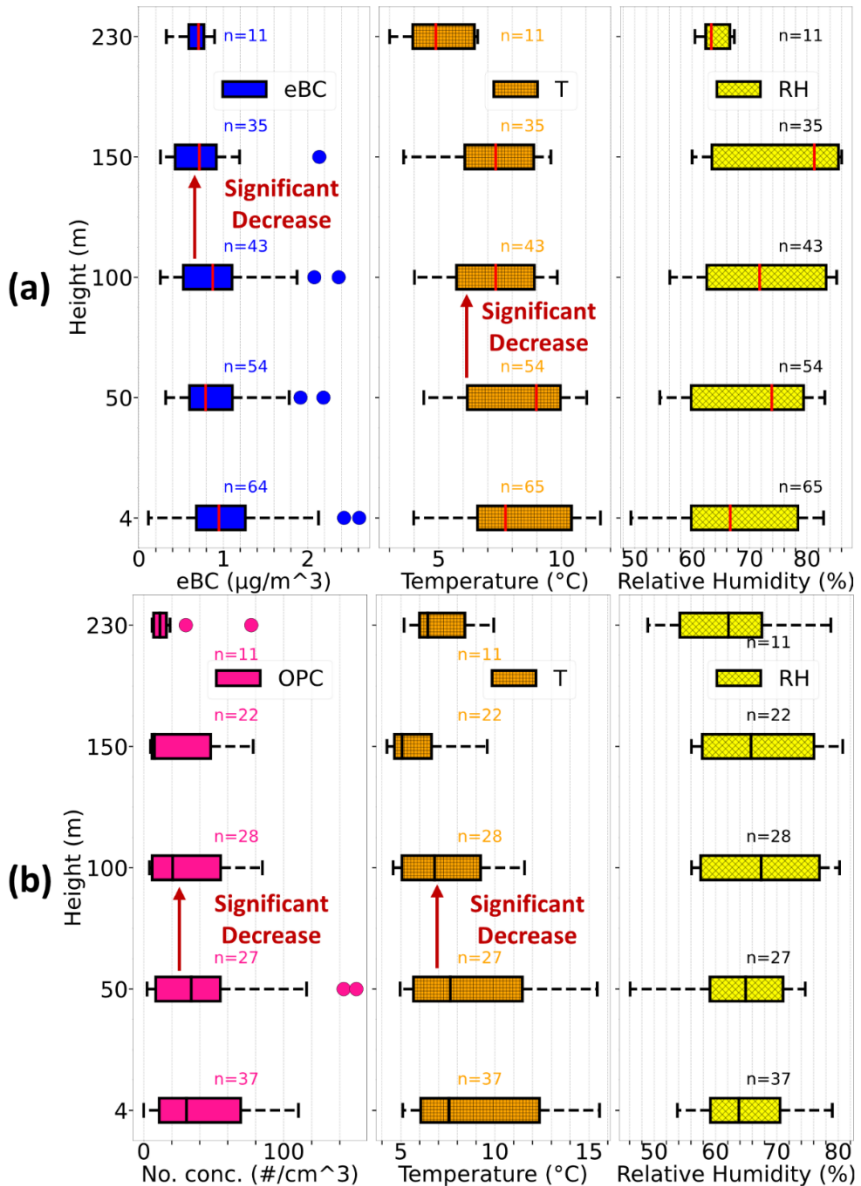
395



396 **Figure 5.** Boxplots of (a) eBC mass concentration and (b) PNC from the drone (full size range used) while hovering at
 397 different altitudes during summer 2023 at NAOK; c) eBC mass concentration and (d) PNC from the drone while
 398 hovering at different altitudes during winter 2024 at NAOK. Boxes show median and IQR; whiskers extend to $1.5 \times \text{IQR}$;
 399 points beyond are outliers. n = number of points (1-min means) per altitude.

400 Simultaneously, the vertical gradient of temperature and RH were examined during the winter campaign
 401 to explain the vertical changes in eBC and PNC. The eBC, PNC, temperature, and RH comparison revealed no
 402 significant temperature variation from the ground to 50 m for both eBC mass and PNC (Figure 6). The nearly
 403 uniform (isothermal) temperature profile ($\Delta T \approx 0.05^\circ\text{C}$ between 4 m and 50 m) indicates very weak vertical
 404 temperature gradients and limited turbulent exchange, which can promote accumulation of eBC and PNC near the
 405 surface. Such near-isothermal conditions correspond to a shallow, stable mixed boundary layer, typical of winter
 406 mornings in mid-latitude regions, when solar heating is too weak to drive convective turbulence and mix the
 407 surface air upward (Steeneveld, 2014). Previous studies reported similar near-surface accumulation of pollutants
 408 under weak or isothermal temperature (Marucci and Carpentieri, 2019; Wang et al., 2018b).

410 The temperature started to decrease with height above 50 m, and the PNCs decreased, while eBC mass
 411 concentrations remained constant up to 100 m despite the temperature changes. This vertical pattern is similar to
 412 the summer measurements, where eBC mass was uniform up to 50 m, and PNC decreased from the ground. This
 413 difference between eBC and PNC with altitude likely reflects particle size and lifetime differences: eBC, mostly
 414 sub-micron, has lower deposition velocities and longer residence times, while larger or semi-volatile particles
 415 dominating PNC are more prone to settling and condensation losses. Deposition velocity increases markedly with
 416 particle size (Donateo et al., 2023), making dry deposition a key driver of size-dependent vertical gradients. This
 417 indicates that differences in particle size may have brought the observed changes in PNC compared to the
 418 unaffected eBC mass concentrations. The consistency across seasons suggests that eBC is well mixed within the
 419 lower mixed layer, while PNC is governed more by local production and removal processes such as coagulation
 420 and hygroscopic growth.



421

422 **Figure 6.** Boxplots of (a) vertical distribution of eBC mass concentration from AE51 without dryer, temperature, and
 423 RH, and (b) vertical distribution of PNC from OPC, temperature, and RH on the drone at rural site NAOK during
 424 winter 2024 . Boxes show median and IQR; whiskers extend to $1.5 \times \text{IQR}$; points beyond are outliers. n = number of
 425 points (1-min means) per altitude.

426 Further, the decrease in eBC mass concentration with height was more pronounced in summer (32 %)
 427 compared to winter (18 %) at NAOK. On the contrary, PNC decreased with height more during winter (39 %)
 428 than in summer (30 %). These contrasting patterns reflect the role of meteorology and emissions: in summer,
 429 deeper boundary layers and convective mixing disperse eBC more aloft, whereas in winter, shallow mixing retains
 430 it near the surface. The steep winter decline of PNC likely arises because heating emissions emit coarser or semi-
 431 volatile particles that are efficiently lost with height, but in summer, new particle formation produces many fine
 432 particles that distribute more uniformly (Gao et al., 2012; Kulmala et al., 2004). While vertical mixing influences
 433 the vertical distribution of particles, the behavior of eBC vertical distributions reflects the combination of particle
 434 size and atmospheric stability rather than primarily depending on vertical mixing alone (Wang et al., 2018). Our
 435 results suggest that at least two aerosol populations of different sizes and sources were measured during the year,

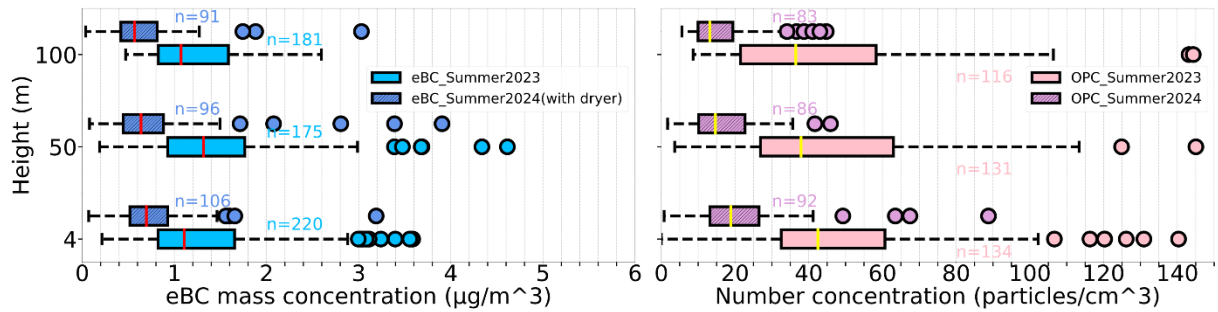
436 thus with different vertical behaviors. This was confirmed by comparison to reference AE33 data from the tower;
437 in winter, biomass/wood burning contributed 48% and 44% of eBC measured at 4 m and 230 m, respectively,
438 leading to a higher absorption Ångström exponent (AAE) of 1.6 and 1.5, respectively, while in summer, fossil
439 fuel combustion (AAE of 1.19 and 1.24, respectively) was the main source of eBC at NAOK, and biomass burning
440 contributing to 18% and 22% of eBC, respectively.

441 **3.3. Aerosol vertical profiles at the urban site**

442 At the urban site, eBC mass concentration and PNC measurements were conducted up to 100 m during summer
443 in two different years – 2023 and 2024. The eBC mass concentrations were measured without the dryer from
444 August 14 to August 20, 2023, and with the dryer from July 18 to July 23, 2024. During both summers, eBC mass
445 concentration and PNC were uniform up to the height of 100m (Figure 7). This consistency can be attributed to
446 several factors. The high number of traffic emission sources at the site contributes to high and relatively stable
447 eBC concentrations in the lower atmosphere, similar to the results of (Liu et al., 2023). Also, enhanced thermal
448 convection and the urban heat island effect facilitate effective vertical mixing (Battaglia et al., 2017). Furthermore,
449 wind shear above 2.0 m/s per 100 m between all the heights (4-50m and 50-100m) during both years supports the
450 vertical transport of pollutants. The combination of convective and mechanical turbulence facilitates the rapid
451 vertical redistribution of aerosols, resulting in a uniform eBC and PNC profile despite strong surface emissions.
452 The presence of local sources in the city is further supported by Czech Hydrometeorological Institute (CHMI)
453 ground-based PM₁₀ observations from nearby Karlín (traffic site) and Kobylisy (urban background) stations,
454 which show higher concentrations and distinct diurnal peaks consistent with local traffic and resuspension activity
455 (Figure S10).

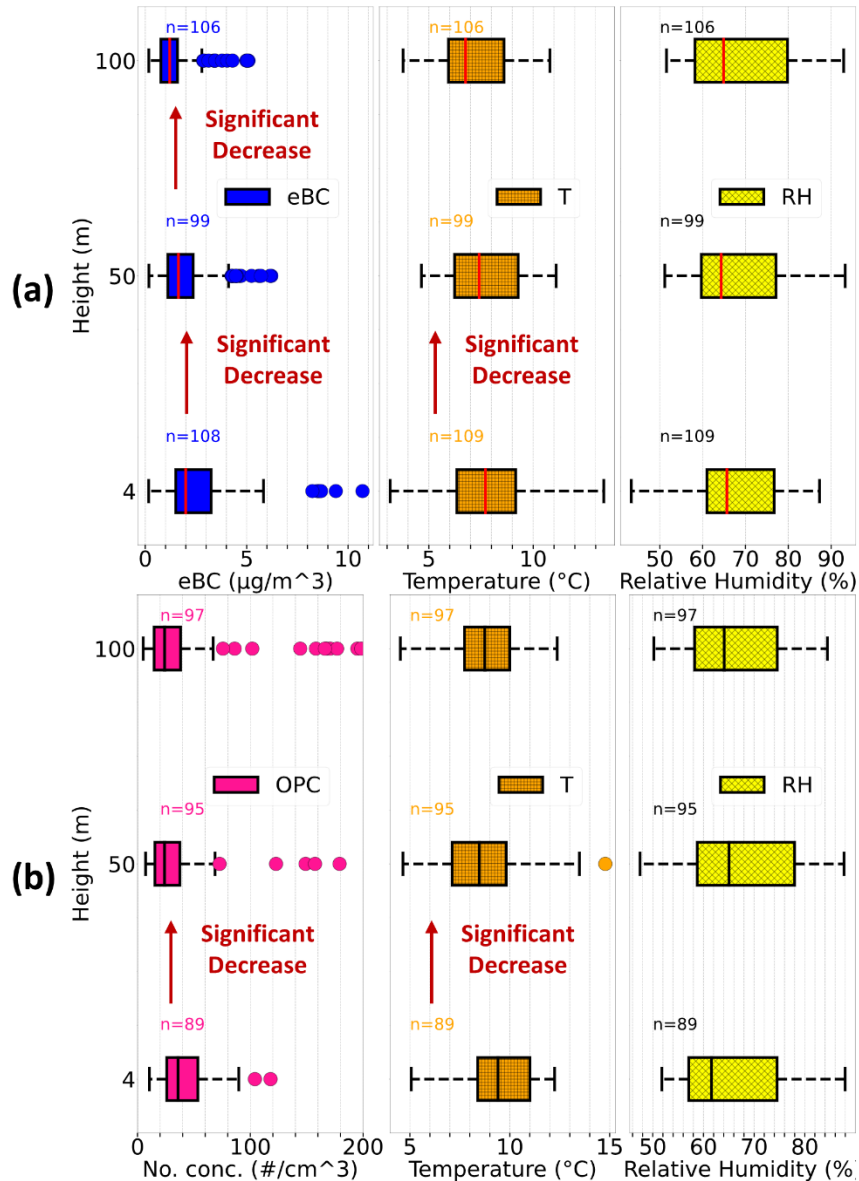
456 The deeper and thermally driven convective boundary layer during summer further increased turbulence,
457 and vertical mixing helped to distribute the particles more evenly within the lower atmospheric layers, thereby
458 homogenizing the particle concentrations. The agreement between summer campaigns with and without the dryer
459 also confirms that under low-to-moderate RH conditions (< 50 %), humidity effects on eBC were minimal in the
460 well-mixed daytime atmosphere. The lower eBC and PNC concentrations observed in summer 2024 compared
461 with summer 2023 can be attributed to meteorology, measurement configuration, and emission changes. Firstly,
462 during 2024, the wind speed (Figure S11) and boundary layer height (Figure S12) were higher, thereby enhancing
463 ventilation and dilution of surface emissions. Secondly, a dryer was used with AE51 during the summer of 2024,
464 thereby reducing the humidity-related overestimation that had affected the summer 2023 measurements. And
465 finally, higher pollutant concentrations were measured in 2023 compared to 2024 in Prague, both by ground-level
466 and 50 m PM data directly at the Prague site (Figure S13), and also at a nearby (2.3 km of the measurement site)
467 CHMI national air quality network station Prague–Karlín station (Figure S14). This independent observation
468 supports the UAV findings and confirms that the interannual difference primarily reflects meteorological
469 variability and reduced local emissions in 2024.

470



471

472 **Figure 7.** Boxplots of (left) eBC concentration from AE51 without a dryer (summer 2023) vs. with a dryer (summer 473 2024) and (right) PNC from OPC at the urban site Prague during summer 2023 and 2024. Boxes show median and 474 IQR; whiskers extend to $1.5 \times \text{IQR}$; points beyond are outliers. n = number of points (1-min means) per altitude.



475

476 **Figure 8.** Boxplots of (a) eBC mass concentration from AE51 without dryer vs. Temperature vs. RH, and (b) PNC from 477 OPC vs. Temperature vs. RH on the drone at Prague from December 12 to December 18, 2023. Boxes show median 478 and IQR; whiskers extend to $1.5 \times \text{IQR}$; points beyond are outliers. n = number of points (1-min means) per altitude.

479 During the winter campaign at Prague from December 12 to December 18, 2023, a significant reduction
480 in both eBC mass concentration and PNC with increasing altitude was observed (Figure 8), contrasting with the
481 summer pattern. Specifically, eBC mass concentration decreased with height up to 100 m, while PNC dropped to
482 50 m from the ground and remained constant between 50 and 100 m. This behavior is primarily influenced by the
483 combination of strong emission sources in urban environments (Figure S10), as described previously, and the
484 weak vertical temperature gradient ($\Delta T \approx 0.06 \text{ }^{\circ}\text{C}$ between 4 m and 50 m), which does not support vertical mixing.
485 During winter, reduced solar heating and long nocturnal cooling produce a shallow, near-isothermal boundary
486 layer which suppresses turbulence and confines pollutants near the surface (Marucci and Carpentieri, 2019; Wang
487 et al., 2018a). The resulting weak turbulent diffusion, rather than a distinct temperature inversion, explains the
488 accumulation of eBC and PNC within the lowest tens of meters. The relatively smaller wind shear (1.1 m/s per
489 100 m between 50 – 100 m) further suppresses vertical mixing, trapping pollutants near the surface (Figure S11).
490 As a result, pollution remains confined closer to the emission sources, leading to higher concentrations near the
491 ground and a more pronounced decrease with height (Kotthaus et al., 2023). Additionally, the urban heat island
492 effect intensifies during stable conditions, causing temperature contrast between urban and rural areas, further
493 reducing the vertical dispersion of pollutants (Haeffelin et al., 2024).

494 Several outliers (extremely high levels) were detected in the eBC mass and PNC. During summer, the
495 outliers can be linked to increased turbulences and daytime convective activities tend to flatten vertical gradients
496 within the mixed layer, yet they can increase temporal variability at a fixed location by intermittently transporting
497 near-surface plumes (e.g., traffic, cooking, construction) to the sampling height. Therefore, these outliers are
498 episodic plume encounters rather than persistent stratification. Fewer outliers were observed at NAOK for eBC
499 and PNC during winter, but more pronounced outliers were present in winter measurements at Prague. This high
500 concentration was due to an elevated winter pollution event between December 13 and 14, 2023. This event was
501 marked by a sharp rise in PM levels, as confirmed by low visibility signals from the drone at 100 m and ongoing
502 PM measurements at the site (Figure S16). The vertical variation and other characteristics of this pollution episode
503 were thus further studied to get a better understanding of the influence of such an event on air quality.

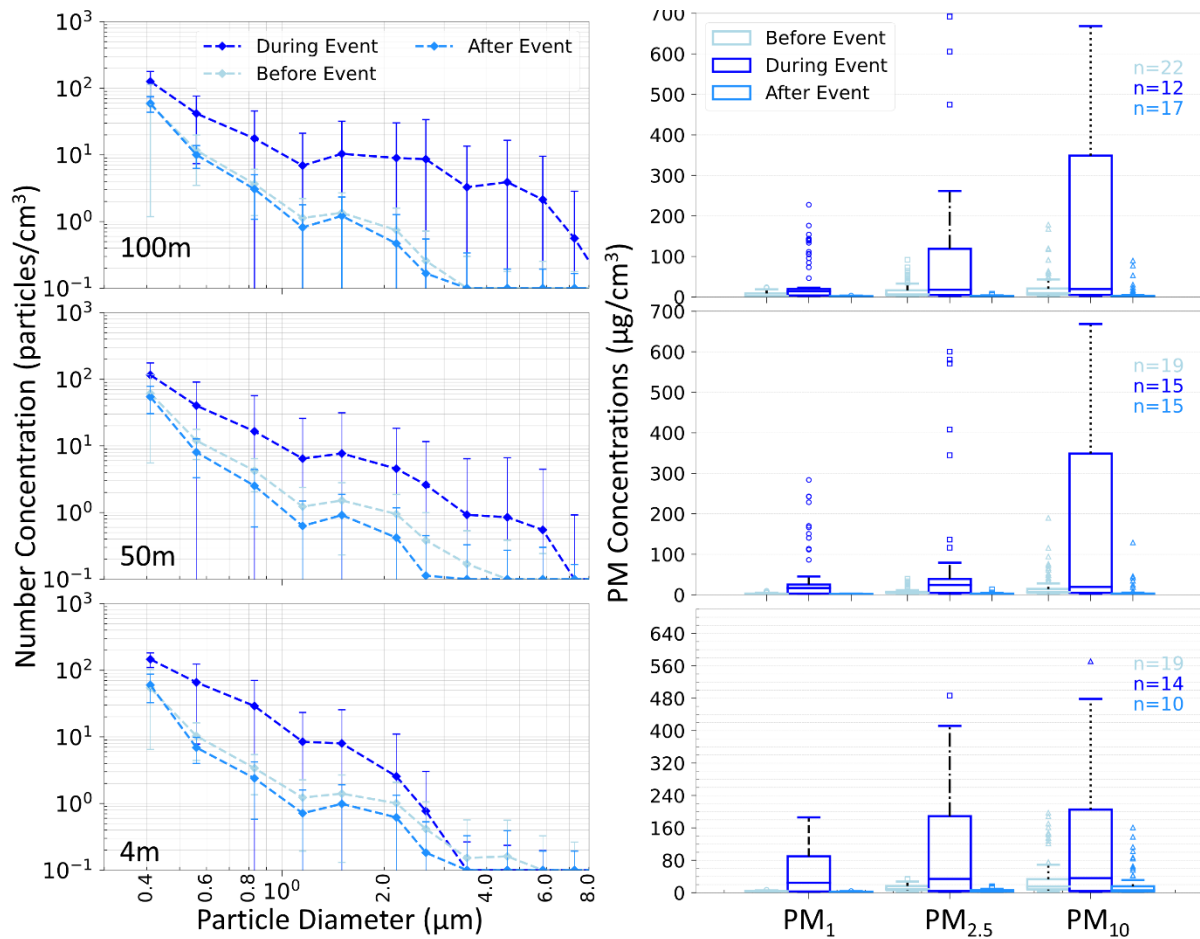
504 **3.4. Vertical variation during an elevated winter pollution event in Prague**

505 An increase in eBC mass concentration and PNC characterized Prague's winter pollution event in December 2023.
506 The event started on December 13th at 13:00 and lasted until the morning of December 14th, 2023. This
507 concentration increase was primarily attributed to a low and stable boundary layer reaching 105 m above the
508 ground (Figure S16). The vertical variation of eBC and PNC, along with the size distribution, was assessed to
509 evaluate the changes one day before (i.e. December 12) and comprised 5 vertical profiles of eBC and 4 profiles
510 of PNC. During the event, 3 profiles for both eBC and PNC were measured, all showing a substantial increase in
511 concentrations at all heights (4m, 50m, and 100m) compared to the period before the pollution episode (Figure
512 S17).

513 The highest increase in eBC concentrations during the event was observed at 100 m, with a 192% (2.5
514 $\mu\text{g}/\text{m}^3$) increase in median eBC levels compared to that before the event. Though less pronounced, the increase in
515 eBC concentration was also seen at 50 m and 4 m, with 130% (1.5 $\mu\text{g}/\text{m}^3$) and 56% (1.7 $\mu\text{g}/\text{m}^3$) increase,
516 respectively. The observed increase in eBC concentration at 100 m, just at the PBL height, suggests that while

517 ground-level emission had some impact, local atmospheric conditions allowed for some degree of vertical
 518 transport of eBC from the above layer, likely influenced by long-distance transported particles. This is supported
 519 by the back trajectory analyses, showing a change in trajectories from southwest to west at the beginning of the
 520 event, associated with transport of continental air masses from higher altitudes (Figure S18). The drone
 521 measurements not only support the measurements at the building (Figure S15), showing higher PM_{2.5} and PM₁₀
 522 concentrations at 50 m compared to 10 m results, but also provide measurements at 100 m, confirming the largest
 523 enhancement in eBC concentration during the event above the building compared to the ground and 50 m. Such
 524 vertical layering is consistent with many winter haze cases where polluted residual-layer air overlies a shallow,
 525 stagnant boundary layer, yielding dual source contributions—local near-surface emissions plus advected/aged
 526 aerosol aloft (Sun et al., 2016).

527 In contrast, PNC showed the highest increase at 4 m and 50 m in comparison to the day before the pollution event,
 528 where PNC increased by 840 % (238 particles/cm³) and 860 % (151 #/cm³), respectively, with a less pronounced
 529 increase at 100 m (460 %, 137 #/cm³). This suggests that some particles, most likely generated from ground
 530 sources, remained concentrated near the surface due to the limited vertical dispersion during the pollution episode.
 531 Prior to the event, eBC concentrations exhibited a significant decrease (by 73 %) from the ground up to 100 m,
 532 and PNC decreased by 38 % between 4 m and 50 m. However, the trend was notably altered during the event,
 533 with no significant change in both eBC and PNC with the height, indicating that daytime mixing has weakened,
 534 allowing accumulation of pollutants throughout the shallow boundary layer.



535

536 **Figure 9. Mean particle number concentration dependence on particle size from OPC on the drone at different heights**
537 **before, during, and after an elevated winter 2023 pollution event in Prague. . n = number of points (1-min means) per**
538 **altitude.**

539 The particle number size distributions at various heights reveal additional information (Figure 9). At 4m,
540 the concentration of particles smaller than 3 μm increased significantly during the event compared to the
541 distribution before the event, highlighting the production and accumulation of small particles near the ground.
542 These particles likely stem from incomplete combustion and secondary formation under stagnant conditions,
543 where condensation of semi-volatile vapors and coagulation processes enhance fine particle numbers (Gani et al.,
544 2019; Zheng et al., 2023). In contrast, at 50 m and 100 m, concentrations of all particles were increased during
545 the event, up to sizes of 10 μm . With the height, mainly the concentration of intermodal fraction, i.e., in sizes
546 between 2.5 and 10 μm , increased in concentrations, potentially indicating contribution from longer distance
547 transported aerosol and mixing processes that redistribute particles vertically. Before the event, particles up to 4
548 μm in diameter were observed near the ground due to winter stable atmospheric conditions (Gani et al., 2019),
549 which restricted vertical mixing and limited dispersion of pollutants. During the event, a substantial increase in
550 larger particles was observed at 100 m (and partly also at 50 m), while almost no change was observed at the
551 ground level concentrations, remaining below 0.1 #/cm³, suggesting contributions from long-range transport
552 disconnected from the ground. A significant increase in PM mass was also observed across all heights (4 m, 50
553 m, and 100 m) (Figure S19). PM₁ and PM_{2.5} dominated the mass concentrations across all heights during the event,
554 while PM₁₀ saw the largest increase at 100 m, again suggesting contributions from coarse particles and vertical
555 mixing.

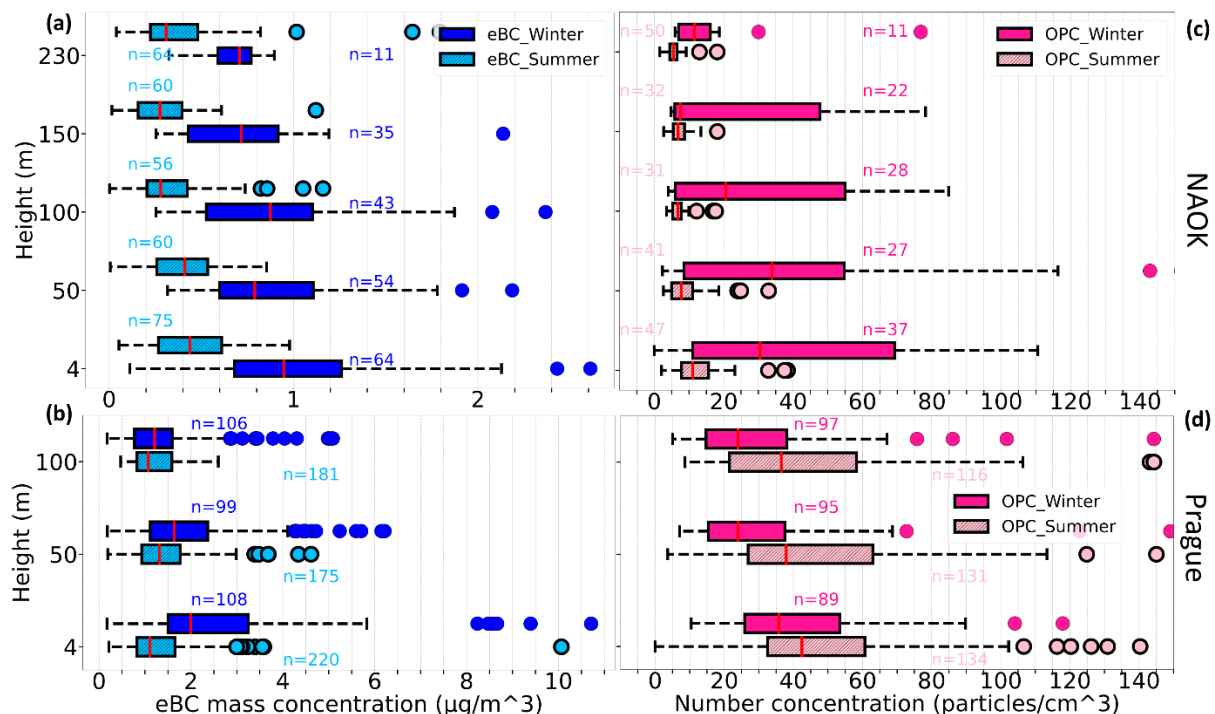
556 **3.5. Seasonal Contrast**

557 The vertical profiles of eBC mass concentration and PNCs during the summer and winter campaigns were
558 compared, revealing significant differences in the seasonal vertical patterns between the two stations.

559 At NAOK in winter, a 100% (0.45 $\mu\text{g}/\text{m}^3$) higher eBC mass concentration up to 50 m was found
560 compared to summer (Figure 10a). This difference can be attributed to more stable atmospheric conditions
561 (isothermal to temperature inversion) hindering vertical mixing and to an increased number of sources during
562 winter. At 100 m, the difference between winter and summer eBC mass concentration surged to 200% (0.5 $\mu\text{g}/\text{m}^3$),
563 as in summer, a decrease in eBC concentrations was observed above 50 m, while it was observed from 100 m in
564 winter. The upward shift of the gradient during winter indicates a shallower mixed layer that traps pollutants
565 within the lowest 100 m. Such seasonal layering of black-carbon aerosols has also been observed in at NAOK
566 (Mbengue et al., 2020). In contrast, during the winter campaign at Prague, eBC mass concentration was 80% (0.88
567 $\mu\text{g}/\text{m}^3$) higher at the ground level compared to summer, but the difference decreased to 24 % (0.32 $\mu\text{g}/\text{m}^3$) at 50
568 m (Figure 10b). No significant difference in eBC mass concentrations in summer and winter was found at 100 m,
569 indicating effective dispersion at this altitude at Prague, likely influenced by local factors such as the surrounding
570 plateau, which alters airflow patterns and enhances the mixing of pollutants above the top of the valley. This
571 suggests that while surface emissions dominate near ground level, mechanical turbulence generated by buildings
572 and local topography enhances mixing aloft, mitigating vertical gradients

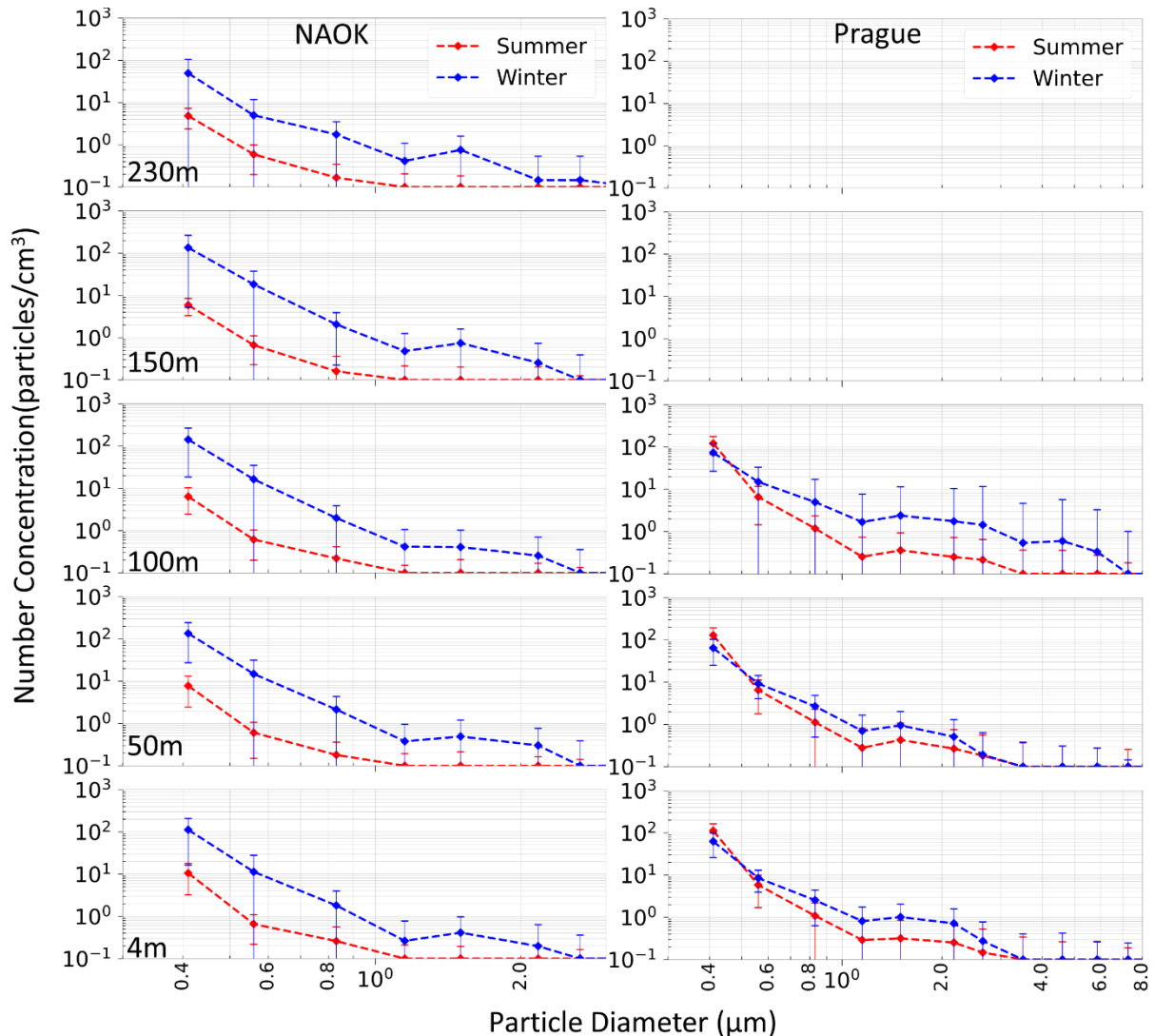
573 For PNC at NAOOK, a 200% (19 $\#/cm^3$) increase was observed at ground level during winter compared
 574 to summer, which extended to 336% (26 $\#/cm^3$) at 50 m and 200% (148 $\#/cm^3$) at 100m (Figure 10c). However,
 575 at 150 m, the winter-summer difference was indistinguishable (differed only by 1 $\#/cm^3$) during the campaign,
 576 suggesting that particles disperse horizontally more rapidly than vertically at this altitude, likely due to
 577 atmospheric stability restricting vertical movements during winter. This is further supported by wind shear values
 578 between 100 – 150 m, which were 1.6 m/s per 100 m during summer, indicating higher turbulence and stronger
 579 vertical mixing. In contrast, winter exhibited lower wind shear (0.5 m/s per 100 m), signaling reduced turbulence
 580 and weaker vertical mixing (Figure S11), favoring horizontal dispersion over vertical transport.

581 In contrast, in Prague, the PNC behaved differently i.e., higher concentration was measured in summer
 582 compared to winter. The particle concentrations decreased with the height more during winter compared to
 583 summer (Figure 10d), with only a small difference at the ground level (15%) (7 $\#/cm^3$) and a higher difference at
 584 50 m and 100 m (36%, i.e. 10 $\#/cm^3$ and 34%, i.e. 12 $\#/cm^3$ respectively).



585
 586 **Figure 10. Boxplots of eBC mass concentration from AE51 and PNC from OPC on the drone during summer 2023 and**
 587 **winter 2024 at (a, c) NAOOK and summer 2023 and winter 2023 at (b, d) Prague. Boxes show median and IQR; whiskers**
 588 **extend to 1.5×IQR; points beyond are outliers. n = number of points (1-min means) per altitude.**

589 To understand these patterns further, particle size distribution was examined for the summer and winter
 590 campaigns at NAOOK and Prague (Figure 11). It is important to note that the size distribution analysis excluded
 591 the high pollution event for Prague to avoid skewed results. At the NAOOK site, both seasons showed a general
 592 decline in concentration as particle size increased; with winter concentrations consistently higher across all sizes
 593 (up to 3 μm), likely due to limited vertical mixing and increased combustion. As a result, in winter, the PNC over
 594 1 $\#/cm^3$ were observed up to 1 μm at all heights, while in summer, the concentrations decreased below 1 $\#/cm^3$
 595 for particles larger than 500 nm.



596

597 **Figure 11. Log-Log plot of the variation of mean particle number concentration with particle size from OPC on the**
 598 **drone at different heights during summer 2023 and winter 2024 at NAOK (left) and summer 2023 and winter 2023 at**
 599 **Prague (right).**

600 At the urban site, Prague, the size distribution analysis showed a significant increase in the average
 601 particle count for particles with sizes between 0.5 – 3 μm during the winter month (Dec, 2023) compared to the
 602 summer month (Aug, 2023) across all heights. Despite this increase, PNC was higher in summer than in winter
 603 (Figure 10d), due to higher summer concentrations in the smallest size bin, $<0.5 \mu\text{m}$ (Figure 11). Although based
 604 on the limited number of flights and counts $< 1 \text{ # cm}^{-3}$ for particles over 1 μm (Figure 11), this finding is consistent
 605 with ground-based observations from the national network (Figure S20), also showing higher concentrations of
 606 PM_{10} in Aug 2023 than in Dec 2023.

607 OPC-N3 due to its detection limit of $\sim 0.3 \mu\text{m}$ cannot directly capture new particle formation events and
 608 the subsequent growth that may be the reason for the increase in concentrations. The photochemistry-related origin
 609 of the summer aerosol in the smallest measurable bins is however supported by the higher concentration of
 610 nitrogen dioxide (NO_2) during the summer (Figure S21), combined with increased sunlight (Figure S22), both of
 611 which promote the photochemical production of secondary particles (Gao et al., 2012; Kulmala et al., 2004).

612 The larger particles (2.5 - 8 μm) showed a more significant increase during winter in Prague, particularly
613 at 100m, further suggesting contributions from regional or long-range transported sources.

614 **4. Summary and conclusions**

615 This study presents a campaign-based analysis of vertical measurements of eBC mass concentration and PNC
616 using drone-based profiling at a rural (NAOK) and an urban (Prague) site in the Czech Republic during different
617 seasons. A comparison of drone-deployed instruments with reference measurements at various heights of fixed
618 observational platforms (tall tower and building) was performed under various RH conditions and RH control
619 strategies.

620 The results show the effectiveness of drones for vertical profiling, offering results comparable to
621 reference instruments at various heights between 0 and 230 m and suggesting the applicability of drone eBC and
622 PNC measurements also in higher altitudes. When mounted on a drone, eBC mass concentrations from AE51 with
623 dryer were comparable at the ground and 230 m with the reference devices. Without the dryer, the eBC mass
624 concentration was overestimated by 276 % and 285% compared to the reference devices on the ground during
625 summer and winter, respectively, attributed to higher ambient RH levels. In comparison, results differ by less than
626 10 % from the reference when using a dryer. Thus, drying significantly reduces measurement discrepancies,
627 highlighting the importance of drying in minimizing the impact of RH, particularly for eBC measurements. While
628 the dryer study demonstrates close agreement on a single day, a multi-day validation with the dryer installed
629 remains a priority for future work, as our findings emphasize the necessity of a drying system even on drone-
630 based measurement platforms.

631 At the rural site (NAOK), eBC mass concentration and PNC decreased with height during both seasons,
632 though the height at which the decrease began was higher in winter than in summer. eBC mass concentrations
633 were uniformly distributed up to the first 50 m in summer and up to 100 m in winter. PNC decreased with height
634 from the ground in summer, while it remained uniform up to 50 m in winter, probably due to weak vertical
635 temperature gradients ($\Delta T \approx 0.05 \text{ }^\circ\text{C}$) and limited turbulent mixing during this season, which also led to higher
636 concentrations of both eBC and PNC compared to summer. The higher concentrations during winter at NAOK
637 were primarily driven by fine particles (PM_1) associated with combustion sources such as residential heating.
638 However, our results suggest that at least two aerosol populations of different sizes and sources were measured
639 during the year, thus with different vertical behaviors.

640 Conversely, at the urban site (Prague), both eBC and PNC were more uniform across altitudes in summer,
641 facilitated by local emission sources (supported by local air-quality data) and enhanced vertical mixing driven by
642 the urban heat island effect. eBC mass concentration and PNC in winter decrease with height, reflecting limited
643 vertical mixing due to near-isothermal conditions ($\Delta T \approx 0.06 \text{ }^\circ\text{C}$) and weak wind shear. PNC was higher in
644 summer, likely due to increased secondary particle formation driven by elevated levels of gaseous precursors and
645 photochemical reactions. These seasonal differences emphasize the interplay between emission strength,
646 boundary-layer dynamics, and secondary formation processes in shaping vertical aerosol patterns.

647 During a winter high pollution event in Prague, both eBC and PNC concentrations increased, with long-
648 range transport contributing to high eBC mass at 100m, while PNC remained concentrated near the surface. The

649 largest enhancement aloft coincided with the estimated boundary-layer top, suggesting entrainment of aged,
650 transported aerosols above a shallow mixing layer, while near-surface PNC reflected trapped local emissions.
651 These emphasize the dynamic interaction of local emissions, atmospheric stability, and long-range transport
652 aerosols in shaping vertical concentration profiles, undecipherable by only ground-based measurements. Using
653 drone-based measurements to capture vertical variation in air quality offers valuable insights into pollutant
654 dynamics.

655 While the measurements presented here offer new insights into the vertical variability of eBC and PNC
656 at rural and urban sites, they represent short-term case studies under specific meteorological and seasonal
657 conditions. Therefore, the observed vertical structures and seasonal contrasts should be interpreted as site-specific
658 patterns rather than generalized tendencies. Nonetheless, the study demonstrates the capability of UAV-based
659 systems to capture vertical pollutant gradients with high spatial resolution, highlighting their potential for
660 complementing long-term monitoring and model validation efforts.

661 **Author contribution**

662 KJ, DB, and NZ designed the experiments. KJ carried out all the experiments. KJ was also responsible for
663 conceptualization, methodology, validation, formal analysis, investigation, data curation, visualization, and
664 writing of the original draft. DB contributed to methodology and writing – review & editing. NZ was responsible
665 for validation, supervision, and writing – review & editing. SM was responsible for data curation and contributed
666 to writing – review & editing. VZ contributed to writing – review & editing, funding acquisition, and resources.

667 **Data availability**

668 The dataset including drone measured data and from reference devices and meteorological instruments, covering
669 both rural and urban sites across different seasons is available at JULAHA, KAJAL (2025),
670 “Drone_rural_urban”, Mendeley Data, V1, doi: 10.17632/snbp6w49v9.1

671 **Acknowledgment**

672 We gratefully acknowledge the financial support provided by the National Research Infrastructure Support Project
673 - ACTRIS Participation of the Czech Republic (ACTRIS-CZ LM2023030) and CzeCOS (LM2023048), funded
674 by the Ministry of Education, Youth and Sports of the Czech Republic, and the Czech Science Foundation under
675 grant 24-10768S, ICPF Internal Grant Agency (IGA - 028001) and Charles University Grant Agency (grant
676 number 98124). We also thank colleagues from the Košetice observatory and Department of Atmospheric Physics,
677 Prague, for providing the meteorological data. Special Thanks to our technicians, Petr Roztočil and Rohit, for
678 preparing the Arduino datalogger and Airstream Dryer.

679 **References**

680 Alas, H. D. C., Müller, T., Weinhold, K., Pfeifer, S., Glojek, K., Gregorič, A., Močník, G., Drinovec, L., Costabile,
681 F., Ristorini, M., and Wiedensohler, A.: Performance of microAethalometers: Real-world Field Intercomparisons
682 from Multiple Mobile Measurement Campaigns in Different Atmospheric Environments, *Aerosol Air Qual. Res.*,
683 20, 2640–2653, <https://doi.org/10.4209/aaqr.2020.03.0113>, 2020.

684 Metrostav: <https://www.metrostav.cz/en/segments/tunnelling/references/28-blanka-tunnel-complex>, last access:
685 11 December 2024.

686 Babu, S. S., Moorthy, K. K., Manchanda, R. K., Sinha, P. R., Satheesh, S. K., Vajja, D. P., Srinivasan, S., and
687 Kumar, V. H. A.: Free tropospheric black carbon aerosol measurements using high altitude balloon: Do BC layers

688 build “their own homes” up in the atmosphere?: FREE TROPOSPHERIC BLACK CARBON AEROSOL,
689 *Geophys. Res. Lett.*, 38, n/a-n/a, <https://doi.org/10.1029/2011GL046654>, 2011.

690 Barbieri, L., Kral, S. T., Bailey, S. C. C., Frazier, A. E., Jacob, J. D., Reuder, J., Brus, D., Chilson, P. B., Crick,
691 C., Detweiler, C., Doddi, A., Elston, J., Foroutan, H., González-Rocha, J., Greene, B. R., Guzman, M. I., Houston,
692 A. L., Islam, A., Kemppinen, O., Lawrence, D., Pillar-Little, E. A., Ross, S. D., Sama, M. P., Schmale, D. G.,
693 Schuyler, T. J., Shankar, A., Smith, S. W., Waugh, S., Dixon, C., Borenstein, S., and de Boer, G.: Intercomparison
694 of Small Unmanned Aircraft System (sUAS) Measurements for Atmospheric Science during the LAPSE-RATE
695 Campaign, *Sensors*, 19, 2179, <https://doi.org/10.3390/s19092179>, 2019.

696 Battaglia, M. A., Douglas, S., and Hennigan, C. J.: Effect of the Urban Heat Island on Aerosol pH, *Environ. Sci.*
697 *Technol.*, 51, 13095–13103, <https://doi.org/10.1021/acs.est.7b02786>, 2017.

698 Bezantakos, S., Costi, M., Barmpounis, K., Antoniou, P., Vouterakos, P., Kelethis, C., Sciare, J., and Biskos, G.:
699 Qualification of the Alphasense optical particle counter for inline air quality monitoring, *Aerosol Science and*
700 *Technology*, 55, 361–370, 2020.

701 Boer, G. de, Diehl, C., Jacob, J., Houston, A., Smith, S. W., Chilson, P., Schmale, D. G., Intrieri, J., Pinto, J.,
702 Elston, J., Brus, D., Kemppinen, O., Clark, A., Lawrence, D., Bailey, S. C. C., Sama, M. P., Frazier, A., Crick,
703 C., Natalie, V., Pillar-Little, E., Klein, P., Waugh, S., Lundquist, J. K., Barbieri, L., Kral, S. T., Jensen, A. A.,
704 Dixon, C., Borenstein, S., Hesselius, D., Human, K., Hall, P., Argrow, B., Thornberry, T., Wright, R., and Kelly,
705 J. T.: Development of Community, Capabilities, and Understanding through Unmanned Aircraft-Based
706 Atmospheric Research: The LAPSE-RATE Campaign, <https://doi.org/10.1175/BAMS-D-19-0050.1>, 2020.

707 Bond, T. C., Doherty, S. J., Fahey, D. W., Forster, P. M., Berntsen, T., DeAngelo, B. J., Flanner, M. G., Ghan, S.,
708 Kärcher, B., and Koch, D.: Bounding the role of black carbon in the climate system: A scientific assessment,
709 *Journal of geophysical research: Atmospheres*, 118, 5380–5552, 2013.

710 Brady, J. M., Stokes, M. D., Bonnardel, J., and Bertram, T. H.: Characterization of a Quadrotor Unmanned Aircraft
711 System for Aerosol-Particle-Concentration Measurements, *Environ. Sci. Technol.*, 50, 1376–1383,
712 <https://doi.org/10.1021/acs.est.5b05320>, 2016.

713 Brus, D., Gustafsson, J., Vakkari, V., Kemppinen, O., de Boer, G., and Hirsikko, A.: Measurement report:
714 Properties of aerosol and gases in the vertical profile during the LAPSE-RATE campaign, *Atmospheric Chemistry
715 and Physics*, 21, 517–533, <https://doi.org/10.5194/acp-21-517-2021>, 2021.

716 Brus, D., Le, V., Kuula, J., and Doulgeris, K.: Data collected by a drone backpack for air quality and atmospheric
717 state measurements during Pallas Cloud Experiment 2022 (PaCE2022), *Earth System Science Data Discussions*,
718 2025, 1–14, 2025.

719 Cai, J., Yan, B., Kinney, P. L., Perzanowski, M. S., Jung, K.-H., Li, T., Xiu, G., Zhang, D., Olivo, C., and Ross,
720 J.: Optimization approaches to ameliorate humidity and vibration related issues using the microAeth black carbon
721 monitor for personal exposure measurement, *Aerosol Science and Technology*, 47, 1196–1204, 2013.

722 Cappelletti, D., Petroselli, C., Mateos, D., Herreras, M., Ferrero, L., Losi, N., Gregorić, A., Frangipani, C., La
723 Porta, G., and Lonardi, M.: Vertical profiles of black carbon and nanoparticles pollutants measured by a tethered
724 balloon in Longyearbyen (Svalbard islands), *Atmospheric Environment*, 290, 119373, 2022.

725 Chacón-Mateos, M., Laquai, B., Vogt, U., and Stubenrauch, C.: Evaluation of a low-cost dryer for a low-cost
726 optical particle counter, *Atmospheric Measurement Techniques*, 15, 7395–7410, 2022.

727 Chen, D., Liao, H., Yang, Y., Chen, L., Zhao, D., and Ding, D.: Simulated impacts of vertical distributions of
728 black carbon aerosol on meteorology and PM 2.5 concentrations in Beijing during severe haze events,
729 *Atmospheric Chemistry and Physics*, 22, 1825–1844, 2022.

730 Chi, X., Winderlich, J., Mayer, J.-C., Panov, A. V., Heimann, M., Birmili, W., Heintzenberg, J., Cheng, Y., and
731 Andreae, M. O.: Long-term measurements of aerosol and carbon monoxide at the ZOTTO tall tower to
732 characterize polluted and pristine air in the Siberian taiga, *Atmospheric Chemistry and Physics*, 13, 12271–12298,
733 2013.

734 Chilinski, M. T., Markowicz, K. M., and Markowicz, J.: Observation of vertical variability of black carbon
735 concentration in lower troposphere on campaigns in Poland, *Atmospheric Environment*, 137, 155–170,
736 <https://doi.org/10.1016/j.atmosenv.2016.04.020>, 2016.

737 Corrigan, C., Roberts, G., Ramana, M., Kim, D., and Ramanathan, V.: Capturing vertical profiles of aerosols and
738 black carbon over the Indian Ocean using autonomous unmanned aerial vehicles, *Atmospheric Chemistry and*
739 *Physics*, 8, 737–747, 2008.

740 CSD: <https://www.rsd.cz/silnice-a-dalnice/scitani-dopravy>, last access: 11 December 2024.

741 Ding, A. J., Huang, X., Nie, W., Sun, J. N., Kerminen, V. -M., Petäjä, T., Su, H., Cheng, Y. F., Yang, X. -Q.,
742 Wang, M. H., Chi, X. G., Wang, J. P., Virkkula, A., Guo, W. D., Yuan, J., Wang, S. Y., Zhang, R. J., Wu, Y. F.,
743 Song, Y., Zhu, T., Zilitinkevich, S., Kulmala, M., and Fu, C. B.: Enhanced haze pollution by black carbon in
744 megacities in China, *Geophysical Research Letters*, 43, 2873–2879, <https://doi.org/10.1002/2016GL067745>,
745 2016.

746 Donateo, A., Pappaccogli, G., Famulari, D., Mazzola, M., Scoto, F., and Decesari, S.: Characterization of size-
747 segregated particles' turbulent flux and deposition velocity by eddy correlation method at an Arctic site,
748 *Atmospheric Chemistry and Physics*, 23, 7425–7445, 2023.

749 Dvorská, A., Sedlák, P., Schwarz, J., Fusek, M., Hanuš, V., Vodička, P., and Trusina, J.: Atmospheric station
750 Křešín u Pacova, Czech Republic—a Central European research infrastructure for studying greenhouse gases,
751 aerosols and air quality, *Advances in Science and Research*, 12, 79–83, 2015.

752 Ferrero, L., Ritter, C., Cappelletti, D., Moroni, B., Močnik, G., Mazzola, M., Lupi, A., Becagli, S., Traversi, R.,
753 and Cataldi, M.: Aerosol optical properties in the Arctic: The role of aerosol chemistry and dust composition in a
754 closure experiment between Lidar and tethered balloon vertical profiles, *Science of the total environment*, 686,
755 452–467, 2019.

756 Gani, S., Bhandari, S., Seraj, S., Wang, D. S., Patel, K., Soni, P., Arub, Z., Habib, G., Hildebrandt Ruiz, L., and
757 Apte, J. S.: Submicron aerosol composition in the world's most polluted megacity: the Delhi Aerosol Supersite
758 study, *Atmospheric Chemistry and Physics*, 19, 6843–6859, 2019.

759 Gao, J., Chai, F., Wang, T., Wang, S., and Wang, W.: Particle number size distribution and new particle formation:
760 New characteristics during the special pollution control period in Beijing, *Journal of Environmental Sciences*, 24,
761 14–21, [https://doi.org/10.1016/S1001-0742\(11\)60725-0](https://doi.org/10.1016/S1001-0742(11)60725-0), 2012.

762 Good, N., Möller, A., Peel, J. L., and Volckens, J.: An accurate filter loading correction is essential for assessing
763 personal exposure to black carbon using an Aethalometer, *J Expo Sci Environ Epidemiol*, 27, 409–416,
764 <https://doi.org/10.1038/jes.2016.71>, 2017.

765 Haeffelin, M., Ribaud, J.-F., Kotthaus, S., Dupont, J.-C., Lemonsu, A., and Masson, V.: Effect of nocturnal urban
766 boundary layer stability and mixing on temperature contrasts between built-up environments and urban parks,
767 *Copernicus Meetings*, <https://doi.org/10.5194/egusphere-egu24-19030>, 2024.

768 Hagan, D. H. and Kroll, J. H.: Assessing the accuracy of low-cost optical particle sensors using a physics-based
769 approach, *Atmospheric Measurement Techniques*, 13, 6343–6355, <https://doi.org/10.5194/amt-13-6343-2020>,
770 2020.

771 Harm-Altstädtter, B., Voß, A., Aust, S., Bärfuss, K., Bretschneider, L., Merkel, M., Pätzold, F., Schlerf, A.,
772 Weinhold, K., Wiedensohler, A., Winkler, U., and Lampert, A.: First study using a fixed-wing drone for
773 systematic measurements of aerosol vertical distribution close to a civil airport, *Frontiers in Environmental*
774 *Science*, 12, <https://doi.org/10.3389/fenvs.2024.1376980>, 2024.

775 Hedworth, H., Page, J., Sohl, J., and Saad, T.: Investigating errors observed during UAV-based vertical
776 measurements using computational fluid dynamics, *Drones*, 6, 253, 2022.

777 Hersbach, H., Bell, B., Berrisford, P., Biavati, G., Horányi, A., Muñoz Sabater, J., Nicolas, J., Peubey, C., Radu,
778 R., and Rozum, I.: ERA5 hourly data on single levels from 1979 to present, *Copernicus climate change service*
779 (c3s) climate data store (cds), 10, 2018.

780 Julaha, K., Ždímal, V., Holubová Šmejkalová, A., Komíneková, K., and Zíková, N.: Boundary layer and mixing
781 layer height: Models vs. Ground-based measurements intercomparison, *Atmospheric Research*, 315, 107897,
782 <https://doi.org/10.1016/j.atmosres.2024.107897>, 2025.

783 Kotthaus, S., Haeffelin, M., Céspedes, J., Van Hove, M., Drouin, M.-A., Dupont, J.-C., and Foret, G.: Urban
784 atmosphere dynamics for air quality applications: Atmospheric boundary layer height and wind profiles from
785 ground-based remote sensing networks, *EGU-13154*, <https://doi.org/10.5194/egusphere-egu23-13154>, 2023.

786 Kulmala, M., Vehkamäki, H., Petäjä, T., Dal Maso, M., Lauri, A., Kerminen, V.-M., Birmili, W., and McMurry,
787 P. H.: Formation and growth rates of ultrafine atmospheric particles: a review of observations, *Journal of Aerosol
788 Science*, 35, 143–176, <https://doi.org/10.1016/j.jaerosci.2003.10.003>, 2004.

789 Lampert, A., Pätzold, F., Asmussen, M. O., Lobitz, L., Krüger, T., Rausch, T., Sachs, T., Wille, C., Sotomayor
790 Zakharov, D., and Gaus, D.: Studying boundary layer methane isotopy and vertical mixing processes at a rewetted
791 peatland site using an unmanned aircraft system, *Atmospheric Measurement Techniques*, 13, 1937–1952, 2020.

792 Lee, J.: Performance test of microaeth® AE51 at concentrations lower than 2 µg/m³ in indoor laboratory, *Applied
793 Sciences*, 9, 2766, 2019.

794 Li, J., Von Salzen, K., Peng, Y., Zhang, H., and Liang, X.: Evaluation of black carbon semi–direct radiative effect
795 in a climate model, *JGR Atmospheres*, 118, 4715–4728, <https://doi.org/10.1002/jgrd.50327>, 2013.

796 Liang, Y., Wu, C., Wu, D., Liu, B., Li, Y. J., Sun, J., Yang, H., Mao, X., Tan, J., and Xia, R.: Vertical distributions
797 of atmospheric black carbon in dry and wet seasons observed at a 356-m meteorological tower in Shenzhen, South
798 China, *Science of the Total Environment*, 853, 158657, 2022.

799 Liu, B., Wu, C., Ma, N., Chen, Q., Li, Y., Ye, J., Martin, S. T., and Li, Y. J.: Vertical profiling of fine particulate
800 matter and black carbon by using unmanned aerial vehicle in Macau, China, *Science of The Total Environment*,
801 709, 136109, <https://doi.org/10.1016/j.scitotenv.2019.136109>, 2020.

802 Liu, H., Pan, X., Lei, S., Zhang, Y., Du, A., Yao, W., Tang, G., Wang, T., Xin, J., and Li, J.: Vertical distribution
803 of black carbon and its mixing state in the urban boundary layer in summer, *Atmospheric Chemistry and Physics*,
804 23, 7225–7239, 2023.

805 Marucci, D. and Carpentieri, M.: Effect of local and upwind stratification on flow and dispersion inside and above
806 a bi-dimensional street canyon, *Building and Environment*, 156, 74–88, 2019.

807 Masey, N., Ezani, E., Gillespie, J., Sutherland, F., Lin, C., Hamilton, S., Heal, M. R., and Beverland, I. J.: Consistency of urban background black carbon concentration measurements by portable AE51 and reference
808 AE22 aethalometers: Effect of corrections for filter loading, *Aerosol and Air Quality Research*, 20, 329–340,
809 2020.

810 Mbengue, S., Serfozo, N., Schwarz, J., Ziková, N., Holubová, S. A., and Holoubek, I.: Characterization of
811 Equivalent Black Carbon at a regional background site in Central Europe: Variability and source apportionment☆,
812 *Environmental Pollution*, 260, 113771, <https://doi.org/10.1016/j.envpol.2019.113771>, 2020.

813 Mbengue, S., Zikova, N., Schwarz, J., Vodička, P., Šmejkalová, A. H., and Holoubek, I.: Mass absorption cross-
814 section and absorption enhancement from long term black and elemental carbon measurements: A rural
815 background station in Central Europe, *Science of The Total Environment*, 794, 148365,
816 <https://doi.org/10.1016/j.scitotenv.2021.148365>, 2021.

817 Mbengue, S., Vodička, P., Komíneková, K., Zíková, N., Schwarz, J., Prokeš, R., Suchánková, L., Julaha, K.,
818 Ondráček, J., and Holoubek, I.: Different approaches to explore the impact of COVID-19 lockdowns on
819 carbonaceous aerosols at a European rural background site, *Science of The Total Environment*, 164527, 2023.

820 Miyakawa, T., Mordovskoi, P., and Kanaya, Y.: Evaluation of black carbon mass concentrations using a
821 miniaturized aethalometer: Intercomparison with a continuous soot monitoring system (COSMOS) and a single-
822 particle soot photometer (SP2), *Aerosol Science and Technology*, 54, 811–825, 2020.

824 Mizera, J., Havelcová, M., Machovič, V., Borecká, L., and Vörös, D.: Neutron Activation Analysis in Urban
825 Geochemistry: Impact of Traffic Intensification after Opening the Blanka Tunnel Complex in Prague, Minerals,
826 12, 281, <https://doi.org/10.3390/min12030281>, 2022.

827 Moteki, N.: Climate-relevant properties of black carbon aerosols revealed by in situ measurements: a review, Prog
828 Earth Planet Sci, 10, 12, <https://doi.org/10.1186/s40645-023-00544-4>, 2023.

829 Myhre, G., Myhre, C. E. L., Samset, B. H., and Storelvmo, T.: Aerosols and their relation to global climate and
830 climate sensitivity, Nature Education Knowledge, 4, 7, 2013.

831 Nurowska, K. and Markowicz, K. M.: Determination of hygroscopic aerosol growth based on the OPC-N3
832 counter, Atmosphere, 15, 61, 2023.

833 Nurowska, K., Mohammadi, M., Malinowski, S., and Markowicz, K.: Applicability of the low-cost OPC-N3
834 optical particle counter for microphysical measurements of fog, Atmospheric Measurement Techniques, 16,
835 2415–2430, 2023.

836 Petzold, A., Ogren, J. A., Fiebig, M., Laj, P., Li, S.-M., Baltensperger, U., Holzer-Popp, T., Kinne, S., Pappalardo,
837 G., and Sugimoto, N.: Recommendations for reporting "black carbon" measurements, Atmospheric Chemistry
838 and Physics, 13, 8365–8379, 2013.

839 Ramana, M., Ramanathan, V., Feng, Y., Yoon, S., Kim, S., Carmichael, G., and Schauer, J.: Warming influenced
840 by the ratio of black carbon to sulphate and the black-carbon source, Nature Geoscience, 3, 542–545, 2010.

841 Ramanathan, V. and Carmichael, G.: Global and regional climate changes due to black carbon, Nature geoscience,
842 1, 221–227, 2008.

843 Ramatheerthan, S. K., Peiker, J., Crespo, N. M., and Kozubek, M.: Monitoring Extreme Meteorological and
844 Pollution Events in Prague: A Station Data Based Analysis, WDS'24 Proceedings of Contributed Papers —
845 Physics (eds. J. Šafránková and J. Pavlů), 9–18, 2024.

846 Renard, J.-B., Michoud, V., and Giacomoni, J.: Vertical profiles of pollution particle concentrations in the
847 boundary layer above Paris (France) from the optical aerosol counter LOAC onboard a touristic balloon, Sensors,
848 20, 1111, 2020.

849 Samad, A., Vogt, U., Panta, A., and Uprety, D.: Vertical distribution of particulate matter, black carbon and ultra-
850 fine particles in Stuttgart, Germany, Atmospheric Pollution Research, 11, 1441–1450, 2020.

851 Samset, B. H., Myhre, G., Schulz, M., Balkanski, Y., Bauer, S., Berntsen, T. K., Bian, H., Bellouin, N., Diehl, T.,
852 and Easter, R. C.: Black carbon vertical profiles strongly affect its radiative forcing uncertainty, Atmospheric
853 Chemistry and Physics, 13, 2423–2434, 2013.

854 Schulz, H., Zanatta, M., Bozem, H., Leaitch, W. R., Herber, A. B., Burkart, J., Willis, M. D., Kunkel, D., Hoor,
855 P. M., and Abbatt, J. P.: High Arctic aircraft measurements characterising black carbon vertical variability in
856 spring and summer, Atmospheric Chemistry and Physics, 19, 2361–2384, 2019.

857 Schwarz, J. P., Gao, R. S., Fahey, D. W., Thomson, D. S., Watts, L. A., Wilson, J. C., Reeves, J. M., Darbeheshti,
858 M., Baumgardner, D. G., Kok, G. L., Chung, S. H., Schulz, M., Hendricks, J., Lauer, A., Kärcher, B., Slowik, J.
859 G., Rosenlof, K. H., Thompson, T. L., Langford, A. O., Loewenstein, M., and Aikin, K. C.: Single-particle
860 measurements of midlatitude black carbon and light-scattering aerosols from the boundary layer to the lower
861 stratosphere, J. Geophys. Res., 111, 2006JD007076, <https://doi.org/10.1029/2006JD007076>, 2006.

862 Sheskin, D. J.: Handbook of parametric and nonparametric statistical procedures, Chapman and hall/CRC, 2003.

863 Steeneveld, G.-J.: Current challenges in understanding and forecasting stable boundary layers over land and ice,
864 Frontiers in Environmental Science, 2, 41, 2014.

865 Sun, T., Wu, C., Wu, D., Liu, B., Sun, J. Y., Mao, X., Yang, H., Deng, T., Song, L., Li, M., Li, Y. J., and Zhou, Z.: Time-resolved black carbon aerosol vertical distribution measurements using a 356-m meteorological tower in Shenzhen, *Theor Appl Climatol*, 140, 1263–1276, <https://doi.org/10.1007/s00704-020-03168-6>, 2020.

868 Sun, Y., Chen, C., Zhang, Y., Xu, W., Zhou, L., Cheng, X., Zheng, H., Ji, D., Li, J., and Tang, X.: Rapid formation 869 and evolution of an extreme haze episode in Northern China during winter 2015, *Scientific reports*, 6, 27151, 870 2016.

871 Villa, T. F., Salimi, F., Morton, K., Morawska, L., and Gonzalez, F.: Development and validation of a UAV based 872 system for air pollution measurements, *Sensors*, 16, 2202, 2016.

873 Vodička, P., Schwarz, J., Cusack, M., and Ždímal, V.: Detailed comparison of OC/EC aerosol at an urban and a 874 rural Czech background site during summer and winter, *Science of the Total Environment*, 518, 424–433, 2015.

875 Wang, H., Sun, Z., Li, H., Gao, Y., Wu, J., and Cheng, T.: Vertical-distribution characteristics of atmospheric 876 aerosols under different thermodynamic conditions in Beijing, *Aerosol and Air Quality Research*, 18, 2775–2787, 877 2018a.

878 Wang, J., Flagan, R. C., and Seinfeld, J. H.: Diffusional losses in particle sampling systems containing bends and 879 elbows, *Journal of Aerosol Science*, 33, 843–857, 2002.

880 Wang, Q., Sun, Y., Xu, W., Du, W., Zhou, L., Tang, G., Chen, C., Cheng, X., Zhao, X., Ji, D., Han, T., Wang, Z., 881 Li, J., and Wang, Z.: Vertically resolved characteristics of air pollution during two severe winter haze episodes in 882 urban Beijing, China, *Atmospheric Chemistry and Physics*, 18, 2495–2509, <https://doi.org/10.5194/acp-18-2495-2018>, 2018b.

884 Wang, Y., Vogel, J. M., Lin, Y., Pan, B., Hu, J., Liu, Y., Dong, X., Jiang, J. H., Yung, Y. L., and Zhang, R.: 885 Aerosol microphysical and radiative effects on continental cloud ensembles, *Advances in Atmospheric Sciences*, 886 35, 234–247, 2018c.

887 von der Weiden, S.-L., Drewnick, F., and Borrmann, S.: Particle Loss Calculator – a new software tool for the 888 assessment of the performance of aerosol inlet systems, *Atmospheric Measurement Techniques*, 2, 479–494, 889 <https://doi.org/10.5194/amt-2-479-2009>, 2009.

890 Weltje, G. J. and Roberson, S.: Numerical methods for integrating particle-size frequency distributions, 891 *Computers & Geosciences*, 44, 156–167, <https://doi.org/10.1016/j.cageo.2011.09.020>, 2012.

892 Wu, C., Liu, B., Wu, D., Yang, H., Mao, X., Tan, J., Liang, Y., Sun, J. Y., Xia, R., and Sun, J.: Vertical profiling 893 of black carbon and ozone using a multicopter unmanned aerial vehicle (UAV) in urban Shenzhen of South China, 894 *Science of the Total Environment*, 801, 149689, 2021.

895 Xie, C., Xu, W., Wang, J., Wang, Q., Liu, D., Tang, G., Chen, P., Du, W., Zhao, J., and Zhang, Y.: Vertical 896 characterization of aerosol optical properties and brown carbon in winter in urban Beijing, China, *Atmospheric 897 Chemistry and Physics*, 19, 165–179, 2019.

898 Zheng, Y., Miao, R., Zhang, Q., Li, Y., Cheng, X., Liao, K., Koenig, T. K., Ge, Y., Tang, L., and Shang, D.: 899 Secondary formation of submicron and supermicron organic and inorganic aerosols in a highly polluted urban 900 area, *Journal of Geophysical Research: Atmospheres*, 128, e2022JD037865, 2023.

901 Zhu, Y., Wu, Z., Park, Y., Fan, X., Bai, D., Zong, P., Qin, B., Cai, X., and Ahn, K.-H.: Measurements of 902 atmospheric aerosol vertical distribution above North China Plain using hexacopter, *Science of The Total 903 Environment*, 665, 1095–1102, <https://doi.org/10.1016/j.scitotenv.2019.02.100>, 2019.

904